Studying the Effect of the Tail on the Dynamics of a Flapping-Wing MAV using Free-Flight Data

Rijks, Frank; Karasek, Matej; Armanini, Sophie; de Visser, Coen

DOI
10.2514/6.2018-0524

Publication date
2018

Document Version
Accepted author manuscript

Published in
Proceedings of the 2018 AIAA Modeling and Simulation Technologies Conference

Studying the Effect of the Tail on the Dynamics of a Flapping-Wing MAV using Free-Flight Data

F.G.J. Rijks[1], M. Karásek [2], S.F. Armanini [3] and C.C. de Visser [4]

Delft University of Technology, 2629HS Delft, The Netherlands.

The effects of the horizontal tail surface on the longitudinal dynamics of an ornithopter were studied by systematically varying its surface area, aspect ratio and its longitudinal position. The objective is to improve the understanding of the tail effect on the behaviour of the ornithopter and to assess if simple models based on tail geometry can predict steady-state conditions and dynamic behaviour. A data-driven approach was adopted since no suitable theoretical models for ornithopter tail aerodynamics are available. Data was obtained through wind tunnel and free-flight experiments. Fourteen tail geometries were tested, at four positions with respect to the flapping wings. Linearised models were used to study the effects of the tail on dynamic behaviour. The data shows that, within the tested ranges, increasing surface area or aspect ratio increases the steady-state velocity of the platform and improves pitch damping. Results also suggest that the maximum span width of the tail significantly influences the damping properties, especially when the distance between the tail and the flapping wings is large, which likely relates to the induced velocity profile of the flapping wings. Steady-state conditions can be predicted accurately based on tail geometry even when extrapolated slightly outside the original measurement range. Some trends were identified between model parameters and tail geometry, but more research is required before these trends can be applied as a design tool.

Nomenclature

AR	Aspect ratio $(-)$
b	Horizontal tail maximum span width (mm)
b_{LE}	Horizontal tail surface leading edge span width (mm)
c_r	Horizontal tail surface root chord (mm)
c_t	Horizontal tail surface tip chord (mm)
g	Gravitational acceleration $(g = 9.81 ms^{-2})$
I_{yy}	Body moment of inertia $(kg \cdot m^2)$
m	Mass (kg)
P	Parameter covariance matrix
p, q, r	Angular rates in body-fixed reference frame $(rad \cdot s^{-1})$
S	Surface area (cm^2)

[1] MSc Graduate Student, Department of Control & Simulation, Faculty of Aerospace Engineering, Kluyverweg 1, 2629HS Delft, The Netherlands.

[2] Postdoctoral Researcher, Department of Control & Simulation, Faculty of Aerospace Engineering, Kluyverweg 1, 2629HS Delft, The Netherlands.

[3] PhD Student, Department of Control & Simulation, Faculty of Aerospace Engineering, Kluyverweg 1, 2629HS Delft, The Netherlands, AIAA Student Member.

[4] Assistant Professor, Department of Control & Simulation, Faculty of Aerospace Engineering, Kluyverweg 1, 2629HS Delft, The Netherlands, AIAA Member.

u, v, w	Velocities in body-fixed reference frame (ms^{-1})
x_e	Longitudinal position of battery and electronics (mm)
x_h	Tail longitudinal position (mm)
X_i, Z_i, M_i	Stability and control derivatives in standard notation
Δ	Perturbation from steady-state
δ_e	Elevator deflection (deg)
δ_f	Flapping frequency (Hz)
$\hat{\theta}$	Estimated parameter vector
ϕ, θ, ψ	Euler angles (deg)
σ	Standard deviation

I. Introduction

Researchers have been inspired by flying insects and vertebrates for many years due to their enormous aerodynamic capabilities. Their manoeuvrability and flexibility in flight envelope are unparalleled. Insects can quickly transition from hover to fast forward flight and even fly backwards [1]. Flapping-wing flight is a very active field of research and studies involving robotic insect wings have yielded particularly valuable insights into the highly nonlinear and unsteady aerodynamics involved with flapping-wing flight [2–6]. Recent years have seen a significant increase in research into robotic flapping-wing micro aerial vehicles (FWMAVs) in an attempt to exploit the advantages of flapping wings [7–15]. However, due to a still limited understanding of flapping-wing aerodynamics these man-made ornithopters currently cannot match the performance encountered in nature. There is a particular need for simple, yet more complete, dynamic models to design control algorithms and to predict flight performance across a wide range of flight conditions.

Most robotic flappers feature a tail surface for passive stability and to provide easier control through conventional aerodynamic surfaces [16]. This comes at the cost of increased size, higher gust sensitivity and reduced manoeuvrability. For these reasons active wing control, which is needed to achieve tailless FWMAV designs, is a particularly active research field today [10, 11, 17]. However, a tail surface can be beneficial in particular mission scenarios. During fast forward flight, for example, exploiting passive stability may prove to be more energy-efficient than active wing control. Some birds also manipulate their tail geometry for flight control, a feat which may be interesting for future FWMAVs [18]. Even though a tail surface has many potential advantages, the effects of a tail surface on dynamic behaviour have not been studied thoroughly [3, 19]. Numerical methods struggle to capture the complexity of the unsteady, time-varying aerodynamics and its interaction with a tail surface [20]. Theoretical models developed to estimate the aerodynamics of birds' tails have been found to be inaccurate when compared to experimental measurements [18, 21]. Most FWMAV models do not explicitly account for the tail surface [12, 13]. Those models explicitly accounting for the tail are platform-specific and omit the interaction with the flapping wings [8]. A potentially accurate tail aerodynamic model was developed in a recent study, based on the time-varying wake of the flapping wings which was measured using particle image velocimetry (PIV) data, but the resulting aerodynamic tail model remains to be validated [22]. Improving the understanding of the effect of a tail surface and its interaction with the flapping-wing wake could lead to more complete FWMAV models and should benefit the development of robotic ornithopters with improved performance.

System identification is an attractive approach to study the effect of the tail because of the highly complex, nonlinear aerodynamics involved with flapping flight and the current lack of suitable theoretical models of tail aerodynamics. Data can be obtained either from wind tunnel measurements or through free-flight. Free-flight data is the most ideal since the data is acquired in the most realistic setting. Recent developments in on-board data acquisition, in combination with optical tracking data, have opened the door for obtaining high quality data suitable for system identification from free-flight [13, 23–26].

This paper presents the results of a systematic study into the effect of the horizontal tail surface on the flight dynamics of an ornithopter, the DelFly II ([19]), using free-flight and wind tunnel

experiments. Specifically, this study focuses on longitudinal, time-averaged dynamics and stability characteristics. The aim is to apply simple, physically meaningful models to achieve new insights into the influence of the tail. The complete design space of tail geometries is vast. Therefore the scope is limited to three parameters: surface area, aspect ratio and longitudinal position. A modified version of the DelFly II is designed, featuring a modular tail which can be detached in its entirety from the body and which facilitates easy adjustment of the horizontal tail surface and the longitudinal position of the tail.

Wind tunnel experiments were used to obtain measurements both with and without tail surface, attempting estimate the contribution of the tail surface to the total forces and moments. Measurements were also performed in several flight conditions surrounding the steady-state resulting in estimations of stability derivatives with respect to free-stream velocity. Free-flight system identification experiments were conducted using pre-programmed elevator doublet manoeuvres. The free-flight data was used to estimate longitudinal, decoupled linear time-invariant (LTI) models. This model structure is relatively simple and has proven to be effective in predicting time-averaged dynamics of ornithopters [12, 27]. An analysis of the LTI model eigenvalues and parameters was performed to gain insight into the effect of the horizontal tail on the dynamics of an ornithopter. The feasibility of using trends found in the models to predict dynamic properties when using other tail configurations was assessed as well.

The structure of this paper is as follows. Section II discusses the experimental approach taken in this study, including a detailed description of the test platform and a discussion on experiment execution and data processing. This is followed by a discussion of the modelling approach in Section III, presenting the model structure, the methods of parameter estimation and the model validation approach. Results of the experiments are presented and discussed in Section IV. Finally, Section V summarises the most important findings and offers recommendations for future work.

II. Experimental set-up

A. Test platform

The DelFly II is a four-winged flapping-wing micro aerial vehicle (FWMAV) developed at Delft University of Technology, see Figure 1. Development of this FWMAV started in 2005 and one of its main purposes is to study the aerodynamics of flapping wings through experimental methods. The DelFly II is also used extensively for research into autonomous flight capabilities of small MAVs [7]. The wings are arranged in an X-configuration and have a total span width of $280mm$. For a more complete description of the DelFly II, please refer to de Croon et al. [19].

The DelFly II comes in many forms with varying on-board equipment. The platform used in this study is equipped with a Lisa/S autopilot containing an Inertial Measurement Unit (IMU) for data acquisition. The platform is equipped with active LED markers, indicated by red circles in Figure 1(b), for optical tracking purposes. The ornithopter used in this study ranges in mass from $22.8 - 24.3g$, depending on the test configuration.

Some changes were made to the standard design to facilitate an efficient study of the effect of tail geometry. Most importantly, the tail has been redesigned as a modular part of the system which can be detached from the fuselage in its entirety. This allows intermediate fuselage segments to be added or removed to control the longitudinal position of the tail.

The horizontal tail surface consists of a so-called base tail onto which tail geometries of desired size and shape can be attached. This is illustrated in Figure 1. The base tail and elevator surface can be seen in Figure 1(a), the standard tail has been attached to the base tail in Figure 1(b). Due to this design the platform features a smaller elevator surface than the standard DelFly II. This proved to be no problem in terms of excitation during free-flight experiments.

Since the test geometries should fit around the horizontal base piece the minimum size of the tail geometries is constrained by the size of the horizontal base tail. Through flight experience it was found that the base tail alone is too small for stable flight, thus this limitation has little influence on the final results. The base tail and elevator have a total chord length of $48mm$ and a span width of $80mm$, see Figure 2. This was found to provide suitable support for the vertical tail whilst limiting constraints imposed on the horizontal tail designs.

The fuselage is split into a front section and a tail section. A middle segment can be added to adjust the longitudinal position of the tail. Fuselage segments are connected using a guiding pin

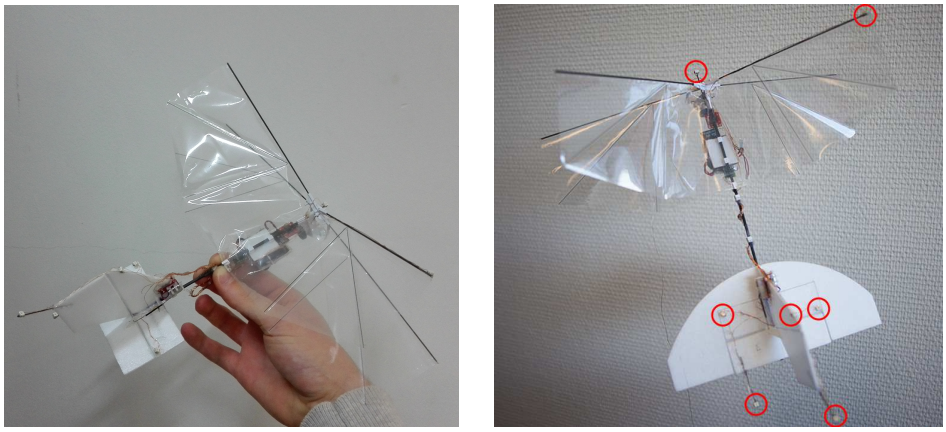

(a) Base tail only. (b) With standard tail.

Fig. 1 Pictures of the FWMAV used in this study, illustrating the modular tail concept.

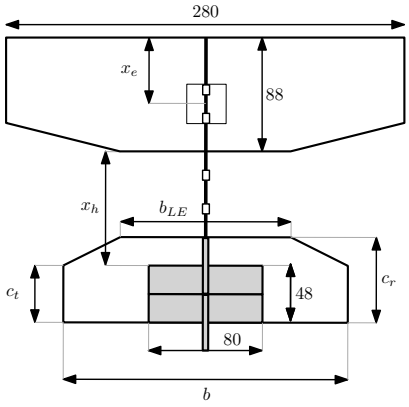

Fig. 2 Geometrical parameters to manipulate tail geometry and position. Figure not to scale.

which slides inside the hollow cross-section of the fuselage, while a bracket prevents the segments from rotating with respect to each other.

B. Test configurations

The number of conceivable tail geometries is enormous. To limit the scope of the study the focus will be on three parameters.

The force generated by an aerodynamic surface scales with its total surface area. In steady aerodynamics this relationship is linear [28]. It is interesting to see if this is also valid for an aerodynamic surface in the wake of flapping wings. Therefore the surface area (S) of the horizontal stabiliser shall be studied.

The second variable is tail aspect ratio (AR). This parameter provides a measure of the aerodynamic efficiency of a wing, for example, in steady aerodynamics. The aspect ratio is defined by Equation (1) [28].

$$AR = \frac{b^2}{S} \tag{1}$$

Finally, it is clear from previous studies that the interaction between flapping wings and tail surface is very complex [18, 20]. PIV experiments show that the wake structure of the DelFly is highly nonlinear and unsteady. Its strength and direction vary with span- and chord-wise position behind the flapping wings [29]. This affects the magnitude of the induced velocity and thus the

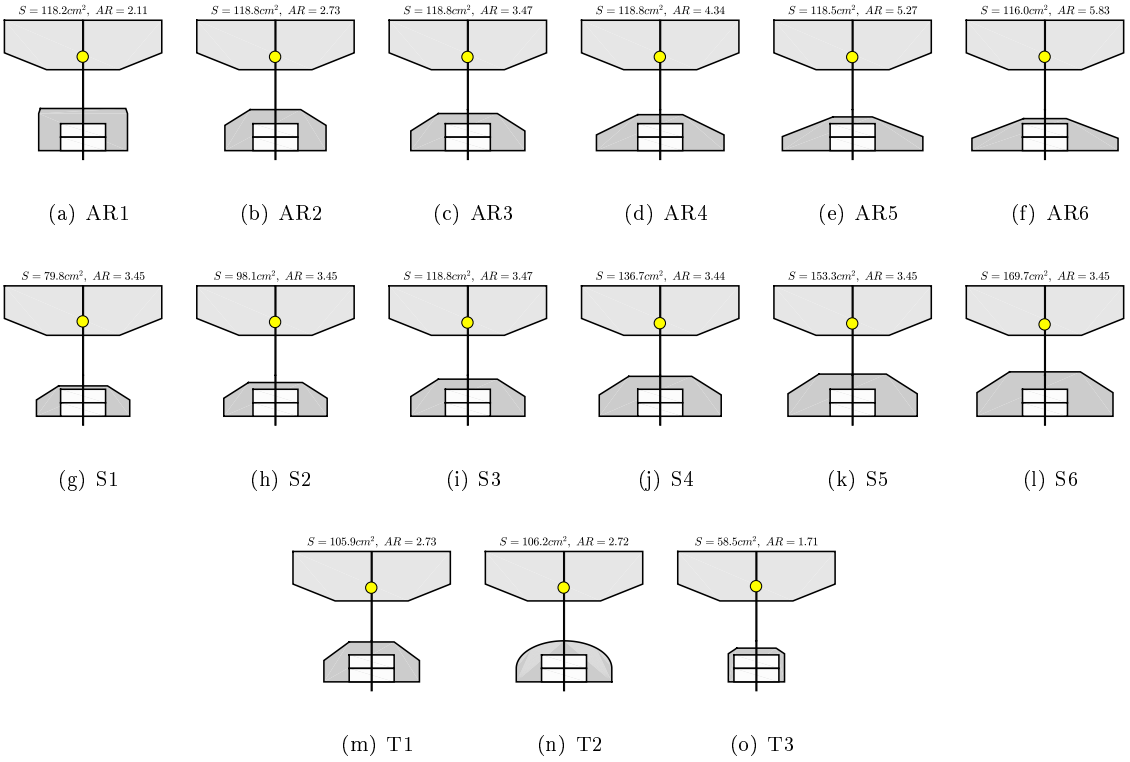

(a) AR1 (b) AR2 (c) AR3 (d) AR4 (e) AR5 (f) AR6

(g) S1 (h) S2 (i) S3 (j) S4 (k) S5 (l) S6

(m) T1 (n) T2 (o) T3

Fig. 3 Tail geometries used in this study. Dot represents the estimated CG position.

Table 1 Fuselage configurations used in the experiments.

Fuselage identifier	a	b	c	d
$x_h(mm)$	57	98	126	114

flow conditions at the tail surface [22]. This warrants an investigation into the effect of longitudinal position on the dynamic behaviour of the FWMAV.

The aforementioned variables are varied systematically to study their effect on the system dynamics. To study surface area and aspect ratio each variable is manipulated whilst keeping the other constant. Figure 2 shows the physical parameters to be manipulated to control the AR, surface area and longitudinal position of the tail surface. x_e denotes the position of the electronics assembly containing the battery and the Lisa/S autopilot. This assembly can slide along the fuselage to provide additional control over the longitudinal position of the centre of gravity (CG).

Figure 3 shows schematics of the tail geometries used in this study. Note that AR3 and S3 in fact share the same geometry, fitting in both test series. The exact physical dimensions are provided in Table A.1, in the appendix. The tail configurations used to test the effect of surface area have a fixed aspect ratio $AR \approx 3.45$, which was found to provide a good range in surface areas that could be covered given the limitations imposed by the base tail. S6 has slightly more than twice the surface area of S1, see Figure 3(g)-3(l). The aspect ratio tails all have a surface area $S \approx 118.2cm^2$. Again this provided the possibility of testing a large range in aspect ratios whilst maintaining the same surface area. The tested aspect ratios range from 2.11 (AR1) to 5.83 (AR6), see Figure 3(a)-3(f).

Figure 3(m), Figure 3(n) and Figure 3(o) show three additional tail surfaces that were tested. T2, in Figure 3(n), is the standard tail surface used for this FWMAV. T1 has practically the same aspect ratio and surface area and was used to assess the effect of changing the leading edge shape to non-elliptical. Within the accuracy of the experimental methods used in this study the response of these two tail configurations was found to be almost identical. Finally, T3 (Figure 3(o)) was used to assess at which point the ornithopter started to show unstable behaviour.

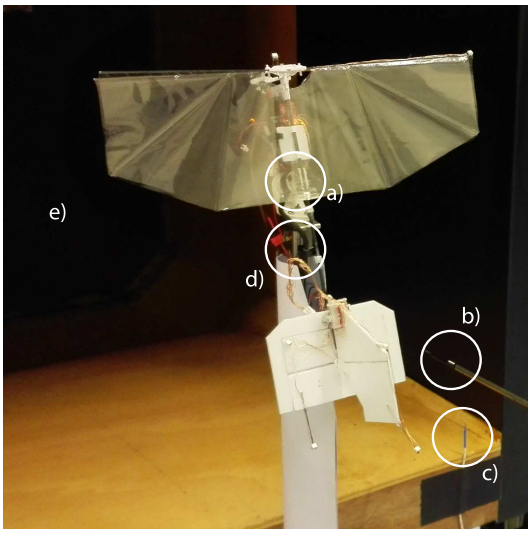

Fig. 4 Picture of the DelFly in the wind tunnel. a) ATI Nano-17 force transducer; b) hot-wire anemometer; c) thermocouple; d) actuated strut; e) open section wind tunnel

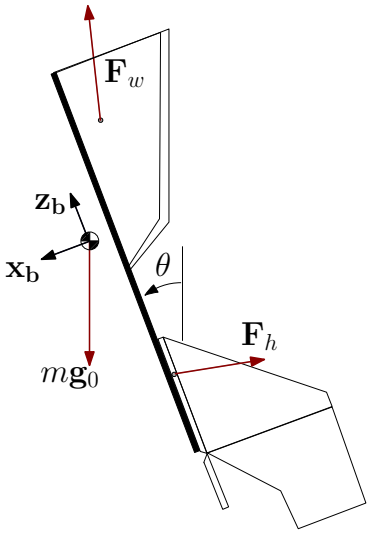

Fig. 5 Free-body diagram of the DelFly in slow forward flight, showing the body-fixed reference frame. $\mathbf{y}_b$ is positive towards the left-hand wing.

A total of four different longitudinal tail positions were tested. Table 1 gives an overview of the fuselage lengths that were used and the corresponding tail positions x_h, defined as the distance from the flapping-wing trailing edge to the leading edge of the base tail, see Figure 2. Throughout the remainder of this paper configurations are denoted by a tail and fuselage identifier, e.g., configuration S3c represents tail S3 at a longitudinal position $x_h = 126mm$.

C. Wind tunnel experiments

Wind tunnel experiments can be used to obtain accurate, high frequency force and moment measurements under pre-defined and well-known conditions. The main reason to conduct wind tunnel experiments is the opportunity to remove the tail without having issues with instability and thereby measure the contribution of the tail to the total forces and moments, i.e., to estimate F_h in Figure 5, by subtracting F_w from the total. Note that the forces in Figure 5 are not to scale. The depicted direction of F_h is loosely based on results by Armanini et al. [22].

Wind tunnel experiments were conducted in the W-tunnel at the TU Delft Faculty of Aerospace Engineering. The W-tunnel is a relatively small wind tunnel designed for low speeds and low turbulence ($\approx 1\%$). For the experiments a $0.6 \times 0.6m$ test section was used. This is large enough to avoid boundary layer effects caused by the walls of the test section to influence the measurements [30]. Figure 4 shows a picture of the ornithopter in the test set-up.

A drawback of wind tunnel experiments is the fact that the MAV is clamped to the force balance, see Figure 4. This has an effect especially on the body x_b force (see Figure 5) due to the absence of oscillations in the pitch attitude which cause aerodynamic damping effects during free-flight [31].

Forces and moments were measured using an *ATI Nano-17* force transducer which measures forces and moments in 6 degrees of freedom (DOF) with a 0.149gram-force resolution. Data is logged with a frequency of $10kHz$ over a duration of two seconds. This corresponds to $24 - 26$ flapping cycles. Flapping cycles are distinguished by use of a Hall-sensor and a magnet attached to the flapping mechanism. This provides the measurement of flapping frequency. The motor RPM is also logged. This can be translated to flapping frequency through the gear ratio ($= 21.33$), providing a redundant measurement. A calibration table is provided at the W-tunnel, correlating wind tunnel RPM to free-stream velocity. In addition, velocity was measured using a hot-wire anemometer. This provides a redundant measurement and the hot-wire system can also detect variations in velocity at high frequency. The pitch angle of the ornithopter was set using an actuated mechanism inside the strut, see Figure 4, and is assumed fixed during a measurement.

For each configuration measurements were performed in the steady state both with tail attached and without the tail. The purpose of these measurements was to obtain an estimate of the contribution of the tail surface to the total forces and moments. Since the steady-state conditions in fact fluctuate during free-flight, the test conditions were also varied, independently, about the steady-state. The pitch angle was varied with $\theta_0 \pm 5$ degrees, the velocity with $V_0 \pm \approx 0.25 m/s$ and the flapping frequency with $\delta_{f,0} \pm \approx 1.4 Hz$. These measurements were performed with the tail attached and allowed estimates of stability derivatives with free-stream velocity, see Section IV B. The steady-state conditions for each configuration were obtained from free-flight prior to the wind tunnel experiments.

D. Free-flight experiments

As mentioned, wind tunnel experiments have some limitations and cannot be used to assess dynamic stability characteristics of a particular configuration [31, 32]. Free-flight experiments are therefore required to thoroughly study the effect of the tail. Only very recently has it become possible to obtain data suitable for system identification from free-flight [12, 25, 27].

Free-flight experiments were conducted in the *CyberZoo* at the Faculty of Aerospace Engineering. The *CyberZoo* is equipped with an optical motion tracking system (henceforth, OptiTrack) consisting of 24 infrared OptiTrack Flex13 cameras. The OptiTrack system tracks the position of active or passive markers within a $10 \times 10 \times 7m$ volume at 120 frames per second. Marker locations on the ornithoper are indicated by the red circles in Figure 1(b). The markers are positioned to give an estimate of the body attitude, the wing angle and control surface deflections [25].

1. Flight test execution

During free-flight experiments the FWMAV was flown manually, though the system identification manoeuvres were pre-programmed and performed automatically. This ensured consistent excitation of the longitudinal dynamics and increased the likelihood of repeatable results. The operator could trigger a manoeuvre using a switch on the transmitter.

The dynamics were excited using doublet pulses on the elevator, which was found to provide the most suitable excitation. The main reason to choose a doublet manoeuvre is its symmetry, which makes it more likely that the ornithopter remains close to its steady-state. This allows the application of linearised models (see Section III). Due to the limited size of the *CyberZoo* it is also an advantage to use the relatively short doublet manoeuvres instead of, for example, 3211 sequences [13].

Through flight testing with the more extreme tail geometries it was found that a 65% elevator deflection with 0.33 second pulses provides sufficient excitation for larger tail geometries whilst not destabilising most of the smaller ones. Experiments for configuration T3 were performed with a 30% deflection doublet since this was the only configuration that was destabilised by larger inputs. For each configuration a single flight was performed with an average flight time of approximately 5-6 minutes, resulting in an average of 21 manoeuvres per flight. It is assumed that each manoeuvre can be treated as an independent experiment.

Before conducting free-flight experiments a calibration between the OptiTrack attitude and the on-board IMU is performed to cope with possible misalignments of the IMU with respect to the body-fixed reference frame [25]. Then an OptiTrack recording and on-board logging can be started. An experiment consists of three steps: (1) trimming the FWMAV to achieve approximately steady, level flight; (2) initiating a manoeuvre; (3) allowing the response to dampen out, during which time no stick input should be given. After some time the ornithopter must be turned to stay inside the tracking volume and the steps are repeated. It is important that sufficient time is allowed for the response to damp out since this provides the most accurate data on the system dynamics.

After each flight the on-board log was downloaded whilst the battery was charging. During the experiments the electronics assembly and battery were fixed in position to minimise the changes made to the ornithopter. Thus, $x_e \approx 52mm$ for all system identification experiments.

For part of the configurations flights were performed with throttle doublet inputs. The input was varied to $\pm 13\%$ of the throttle value at initialisation of the manoeuvre. Pulse duration and experiment execution were the same as for the other system identification experiments. Ultimately

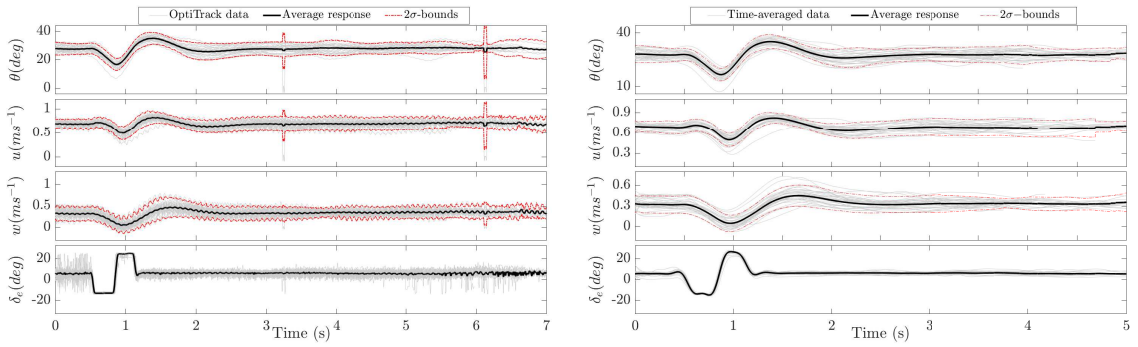

(a) Raw OptiTrack data.

(b) Processed and filtered data.

Fig. 6 Example of raw and processed data for configuration S5b. Overlay of all 23 manoeuvres performed during the flight.

the throttle input provided less efficient excitation of the dynamics. Elevator doublets are a better choice of input since the direct disturbance of the pitching moment gives the most relevant excitation for a study of the tail effect.

2. Data processing

Some processing is required before the data from free-flight experiments can be used for model estimation. This section will briefly discuss the most important elements of data processing. For a more complete description refer to Armanini et al. [26] or Karásek et al. [25].

Data needs to be synchronised in the time-domain since the OptiTrack recording and the on-board IMU data are two individual data-sets. LED markers on the vertical tail and on the rudder, see Figure 1(b), only turn on when on-board data is being logged. This allows the beginning and ending of an on-board log to be observed in the optical tracking data [25]. The OptiTrack data is then interpolated using spline interpolation, from $120Hz$ to $512Hz$, to match the IMU data rate. Euler angles and body-fixed velocities are then estimated using an extended Kalman filter (EKF). The EKF fuses the high frequency data of the IMU and the lower frequency OptiTrack data, which is less prone to drift. For a full description of the Kalman filter see Armanini et al. [26].

Due to the placement of the markers, tracking quality of the elevator angle was sometimes poor. To cope with this, unrealistic elevator angles ($\text{abs}\,(\Delta\delta_e) \geq 25deg$) were removed from the OptiTrack data and the resulting missing values replaced by interpolating between the remaining data points.

Manoeuvres were then automatically isolated using the elevator servo command signal which is logged on-board. A data segment is started 0.5 seconds prior to the beginning of a manoeuvre, to have some run-in time, and lasts until a rudder deflection (i.e., a turn) is detected. The detected manoeuvres were all checked manually to see if the algorithm worked correctly and manually terminated early in case of OptiTrack tracking problems. These sometimes occur when the ornithopter is flown near the edges of the tracking volume.

Finally, the data is filtered using a fourth order low-pass Butterworth filter. The cut-off frequency is chosen at $5Hz$. This was found to be a suitable cut-off frequency to separate the time-averaged signal content from the flapping-related data in previous system identification work performed for this particular ornithopter [27]. Filtering at this cut-off frequency does however cause some rounding of the elevator input data, which may have an effect on the estimated control effectiveness parameters.

An example of the data obtained from free-flight is given in Figure 6. The raw OptiTrack data is shown in Figure 6(a), perfectly illustrating the drastic effect of a tracking problem, showing large spikes in the 2σ bounds. Figure 6(b) shows the same data after processing and filtering. This data is ready to be used for model identification.

III. Modelling

A. Model structure

The model structure used in this study is given in Equation (2). It is a decoupled, longitudinal LTI model. Previous work has shown that the time-averaged dynamics, in a limited domain around steady flight conditions, can be approximated well using LTI models even though flapping-wing MAVs are highly non-linear in nature [12, 13, 33]. This approach is considered valid for ornithopters which have a high enough flapping frequency such that time-scale separation applies [27]. Figure 5 specifies the body-fixed reference frame, which is different from the aerospace convention. Armanini et al. switched to a different reference frame definition in previous work to avoid singularity problems due to the typically large pitch angles assumed by this ornithopter [26].

$$\begin{bmatrix} \Delta\dot{q} \\ \Delta\dot{u} \\ \Delta\dot{w} \\ \Delta\dot{\theta} \end{bmatrix} = \begin{bmatrix} \frac{M_q}{I_{yy}} & \frac{M_u}{I_{yy}} & \frac{M_w}{I_{yy}} & 0 \\ \frac{X_q}{m} - w_0 & \frac{X_u}{m} & \frac{X_w}{m} & -g\cos\theta_0 \\ \frac{Z_q}{m} + u_0 & \frac{Z_u}{m} & \frac{Z_w}{m} & -g\sin\theta_0 \\ 1 & 0 & 0 & 0 \end{bmatrix} \begin{bmatrix} \Delta q \\ \Delta u \\ \Delta w \\ \Delta\theta \end{bmatrix} + \begin{bmatrix} \frac{M_{\delta_e}}{I_{yy}} \\ \frac{X_{\delta_e}}{m} \\ \frac{Z_{\delta_e}}{m} \\ 0 \end{bmatrix} \begin{bmatrix} \Delta\delta_e \end{bmatrix} \tag{2}$$

Initially, flapping frequency, $\Delta\delta_f$, was considered as a second input to the model. However, this did not yield any significant improvement in model accuracy and provided little additional insight into the effect of the tail because responses to throttle input varied only very little between configurations. Also, as discussed before, elevator manoeuvres were found to provide more suitable excitation to study the effect of the tail since it is a direct pitching moment disturbance. For simplicity, flapping frequency was omitted in the final model structure.

The advantage of using the LTI model structure is its simplicity as opposed to, for example, quasi-steady models [4, 34]. LTI models are easier to use for obtaining new insights into the effect of the tail. The model structure is partly physical in nature, i.e., changes in parameter values can be linked to physical changes of the system, but is still relatively easy to interpret.

A drawback of LTI models is their limited validity about a steady-state condition. Moving away from this steady state makes the model less accurate and eventually unusable. It should be kept in mind that the assumption of linearity may be violated during real flight. The LTI model also contains no explicit terms modelling the tail geometry. Thus, it will not always be trivial that changes in parameters are a result of a change in tail geometry. However, for an initial study of the tail effect on the dynamics the LTI model structure is expected to be sufficient.

B. Parameter estimation

Parameters of the LTI model were estimated using a combination of ordinary least squares (OLS) estimation and a maximum likelihood (ML) optimisation step. The OLS estimation is a linear regression problem which always converges to the global optimum but rests on the assumption of error-free regressor measurements. ML estimation on the other hand allows for noise in the measurements but is a nonlinear optimisation problem which is prone to divergence or convergence to local optima. In previous work a combination of these estimation techniques proved to be successful [33]. For a more detailed outline of the parameter estimation approach, see Armanini et al. [27].

Parameters are first estimated using the OLS approach. These estimated parameters are subsequently used as the initial guess for the ML optimisation step. According to a comparison by Armanini et al. the ML optimisation leads to more accurate results if successful, though there is always a risk of divergence [33].

This approach was found to give satisfactory results. Models were estimated for each experiment in a data set, e.g., for each manoeuvre instance, and ML divergence typically occurred for less than two data sets per configuration.

C. Obtaining average models

To compare the dynamic behaviour of the tail geometries it is more convenient to estimate a single, representative model for each configuration. Three approaches to estimate such an average model were attempted.

1. Mean parameter model

The most straightforward approach to estimate an average model for a configuration is to simply take the mean of the parameters estimated in individual models. Since the input used to excite the dynamics is pre-programmed, the excitation of the system is very consistent (see the overlay in Figure 6). This leads to a similar response for each excitation and thus should yield consistent models. Analysing the mean of the model parameters is considered a reasonable first step in determining a representative model. Of course, small disturbances experienced in-flight will lead to variation in the models. The standard deviation of the parameters over the individual models is thus a good measure of the reliability of a certain parameter. The mean and standard deviations of the parameters can also give an indication of the relative importance of that particular parameter on the system dynamics.

2. Weighted mean (WM) model

Taking a simple mean of all the parameters may not be the most accurate method to estimate a representative model, since it assumes that all parameter estimates were equally successful. Due to the nature of the ML optimisation step in the parameter estimation process, this is not necessarily true. Ljung proposes a method which computes a weighted mean (WM) of the parameters by taking into account the covariance matrix of the estimation [35].

Given multiple parameter estimates, obtained from independent sets of data, Equation (3) provides an average parameter set weighted according to the estimated covariance matrices. $\hat{\theta}^i$ represents the parameter estimate for data set i.

$$\hat{\theta} = P \cdot \sum_{i=1}^{n} \left(\left[P^{(i)} \right]^{-1} \cdot \hat{\theta}^i \right), \text{ with } P = \left[\sum_{i=1}^{n} \left[P^{(i)} \right]^{-1} \right]^{-1} \tag{3}$$

This method takes into account that not all estimations are equally good. According to Ljung, the parameter estimate resulting from Equation (3) should be the minimum covariance parameter estimate [35].

3. Averaged time-response (TA) model

Finally, an average model is computed by overlaying the data sets which are to be used for estimation and computing the mean response. A model can then be estimated based on this average response. This approach is assumed valid since the flapping-related content of the data is not taken into account. From Figure 6, the response to the input is very consistent. This is also in line with previous system identification work for the DelFly [13].

Due to the high consistency of the individual manoeuvres performed during an experiment it is considered justified to estimate a model based on the average response as a representative model. Throughout this paper this model shall be indicated as the time-averaged (TA) model.

D. Model validation

1. Approach

Model validation is performed on two levels. First the quality of each individual model is assessed by simulating its response to the measured input. Comparing the model-predicted states to the measured states gives a measure of accuracy for the particular model. Then, the aforementioned averaged models are estimated, using a selection of the accepted data sets, and tested against validation data which was not used to estimate the averaged models.

Three metrics were used to evaluate the quality of individual models: (1) the root mean squared (RMS) error between measured and model-predicted states; (2) the Pearson's correlation coefficient (PCC), see Equation (4), where $\hat{y}$ represents an arbitrary model output state and y_m the respective measured state. The PCC varies from 0 (no correlation) to 1 (full correlation); and (3) the covariance of the parameter estimates.

Table 2 Model validation metrics.

Metric	Threshold
RMS	$RMS \geq 80$ %tile
PCC	mean$(PCC) \leq 0.70$
Covariance	$\lvert\frac{\text{cov}(\hat{\theta})}{\hat{\theta}}\rvert > 1$

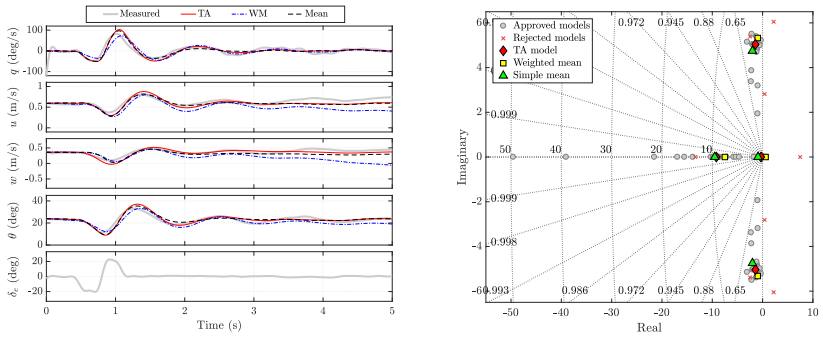

(a) Time response (b) Eigenvalues

Fig. 7 Example of validation results for configuration S1b

$$PCC = \frac{\text{cov}\left(\hat{y}, y_m\right)}{\sigma_{\hat{y}} \cdot \sigma_{y_m}} \tag{4}$$

Suitable thresholds for each validation metric were determined experimentally. The resulting values are given in Table 2. For each model, these metrics are evaluated and each state or parameter exceeding a threshold is flagged. To check if the RMS value of a particular output state is too high it is compared to the RMS values of all individual models. The highest 20% of the RMS values are flagged. The RMS flags are divided by the number of output states (4). The covariance flags are normalised by the total number of parameters. This results in a summed flag value for each model. If the flag value of a model exceeds 1, it is rejected and will not be used to estimate average models for the configuration.

After evaluating the individual models based on the criteria in Table 2, a random selection is made from the accepted models. 70% of the data is selected for identification of averaged models, whilst the remaining 30% of the data is kept for validation.

The averaged models are tested on the remaining validation data to find the most representative one. To evaluate the averaged models, two metrics are used: the mean RMS and the mean PCC values. These results are summed over the total number of validation data sets. The model scoring best on the highest number of data sets is considered to be the most representative model for that particular configuration. The highest fitness models are then used to compare the dynamic characteristics of different tail geometries.

2. Results

Models for all configurations were validated using the aforementioned approach. Figure 7 shows an example of the results for configuration S1b. These results are representative for the bulk of the configurations. In the appendix, Table A.2 gives an overview of the validation results for all configurations.

Figure 7(a) shows the model-predicted time responses versus the measured states for a single validation data set. It is observed that all three models predict the measured states with a reasonable accuracy. There is however a slight instability in the weighted mean (WM) model, caused by a positive real eigenvalue.

Figure 7(b) shows the system eigenvalues on a pole plot. A good clustering of the eigenvalues can be observed, particularly in the complex conjugate eigenvalues. The averaged models show high consistency in the complex conjugate pair of eigenvalues, which are also located around the cluster of the individual models. This gives a measure of confidence into the methods used to obtain the average models. The real eigenvalues are less consistent and show more spread. This was also the case in previous system identification work for this ornithopter and is most likely caused by a lack of excitation in the body z_b-axis [13].

Figure 7(b) also shows the poles of rejected models, which were not used for estimation or validation of the averaged models. In this case the rejected models with unstable complex conjugate pole pairs are a result of ML optimisation divergence. In most cases model rejection was a result of the ML optimisation converging to a local minimum, yielding sub optimal results. Typically less than four individual models are rejected, leaving an average of 12 independent data sets to estimate average models, suggesting that the experiment execution and the estimation process were generally successful.

The three averaged models all perform quite well for the given example. The weighted mean model, however, has a tendency to be drawn towards unstable real poles if these are present in any of the models used to estimate the WM model. Apparently the model parameters of models with an unstable real pole have a very low covariance giving them a high weighting in the computation of the WM model. As a result the WM model shows a slight instability, visible in the time response in Figure 7(a).

Table A.2 shows the validation metrics for configuration S1b. For this configuration, all three average models perform quite well, with a mean $PCC > 0.80$, and mean $RMS = 0.11$ for the TA and mean model. However, the slight instability in the WM model clearly results in higher RMS (0.16) and lower PCC (0.64) values. The TA model scores best and is therefore the most representative model for configuration S1b.

For some configurations the weighted mean model is drawn quite far towards an unstable pole due to more than one model with a positive real eigenvalue in the estimation data. In some cases this leads to poor validation results for the weighted mean model, see Table A.2 for an overview. The simple mean model and the TA model are much less sensitive to models which feature a positive real eigenvalue.

Overall the TA model scored best for a majority of the configurations that were tested. This confirms the consistency of the dynamic excitation and provides additional confidence into proper experiment execution.

IV. Results & discussion

A. Wind tunnel

Figure 8 shows results of the force balance measurements performed in the wind tunnel, in steady-state conditions, as a function of tail geometry. Error bars indicate two times the standard deviation of the forces and moments over a total of 24-26 flapping cycles per measurement. Each steady-state measurement was repeated three times.

It was not possible to identify clear trends consistent with a variable tail geometry from the results in Figure 8 or from force balance results for other longitudinal positions x_h. This made it very difficult to accurately estimate the tail contribution, i.e., F_h in Figure 5, as a function of tail geometry.

This is most likely caused by a combination of the test-setup and the resolution of the sensor that was used. Apparently the force and moment differences are so small that even this high resolution (0.149g-force) sensor has trouble to accurately measure the differences between tails. However, on the small scales involved with this ornithopter these small differences still make a significant difference in dynamic behaviour, as was observed during free-flight (see Section IV B). Furthermore, it is expected that the force balance strut affects the airflow upstream of the tail surface to some extent and thereby influences the measurements. An attempt was made to streamline the strut, see Figure 4, but this is still a drawback and, more importantly, an unknown factor in the measurement.

The difference between tailed and tailless measurements shows opposite trends in Figure 8(a) and Figure 8(b). This also suggests an influence of the force balance strut. With varying x_h the distance between the strut and the tail surface changes which may result in different influences of

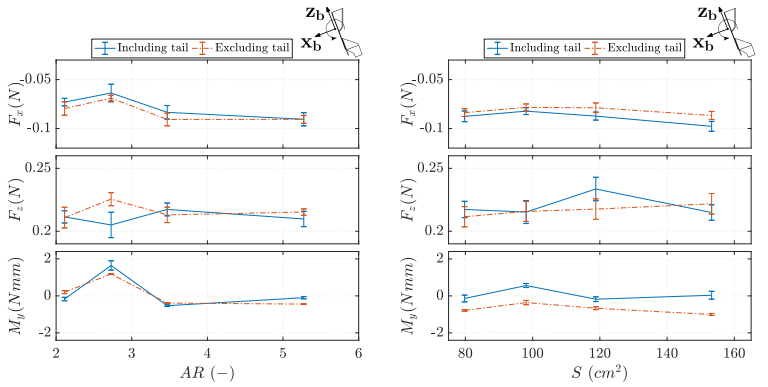

(a) With aspect ratio, $x_h = 98mm$. (b) With surface area, $x_h = 126mm$.

Fig. 8 Wind tunnel results as function of tail geometry. 2σ error-bars.

the strut on the final results. However, the opposite trend may also be caused by a change in tail effectiveness at increased longitudinal distance from the flapping wings. It is currently not possible to differentiate between these two causes since the effect of the strut is unknown.

Previous studies, comparing wind tunnel measurements to free-flight data, pointed out that the force measured in the body x_b-axis is especially influenced by clamping effects [24]. An aerodynamic tail model developed by Armanini et al., using PIV data to model the tail-wake interactions for the DelFly in hover conditions, suggests that the tail is actually generating force almost exclusively in x_b direction, in the range of $0.01 - 0.03N$ [22], which corresponds to the order of magnitude of the results in Figure 8. With the total contribution of the tail in this range it is not unlikely that differences between tail geometries are much smaller and are too small to be measured reliably with the sensor that was available. It can thus be concluded that a change in wind tunnel setup or a more sensitive force balance would be required to accurately estimate the force generated by the tail.

However, it was possible to obtain some estimates of stability derivatives from the wind tunnel results. Figure 18 in Section IV B shows results for X_u, both from the models estimated from free-flight data and derivatives estimated from wind tunnel data. X_u could be estimated from measurements that were performed for free-stream velocities fluctuating about the steady-state ($V_0 \pm \approx 0.25ms^{-1}$). The estimates from wind tunnel data and free-flight are in the same order of magnitude, though the actual values are different. Nevertheless, this provides some measure of confidence in estimates derived both from wind tunnel data and free-flight. More importantly it shows that simple stability derivatives may actually be derived from wind tunnel experiments. However, it also calls for some additional study with regard to the accuracy of both experimental methods.

Figure 18 shows that aspect ratio seems to have no significant effect on X_u. However, a minimal trend is observed with surface area in Figure 18(b), showing a slight increase in magnitude for X_u when the tail surface area is increased. This is as expected, since X_u can be interpreted as the drag force as a function of forward velocity, which is usually influenced by the surface area of the translating body.

B. Free-flight

1. Effect on steady-state

Despite no significant trends to be observed in the wind tunnel results, the tail geometry is still expected to affect the magnitude of the tail force F_h. Assuming that the force generated by the flapping wings (F_w) initially remains unchanged, this would result in a different moment equilibrium and therefore different steady-state conditions, see Figure 5. The effect of the horizontal tail aspect ratio on the steady-state conditions is shown in Figure 9. Linear fits were estimated using three of the configurations, leaving one configuration to validate if steady-state conditions may be predicted based on tail geometry.

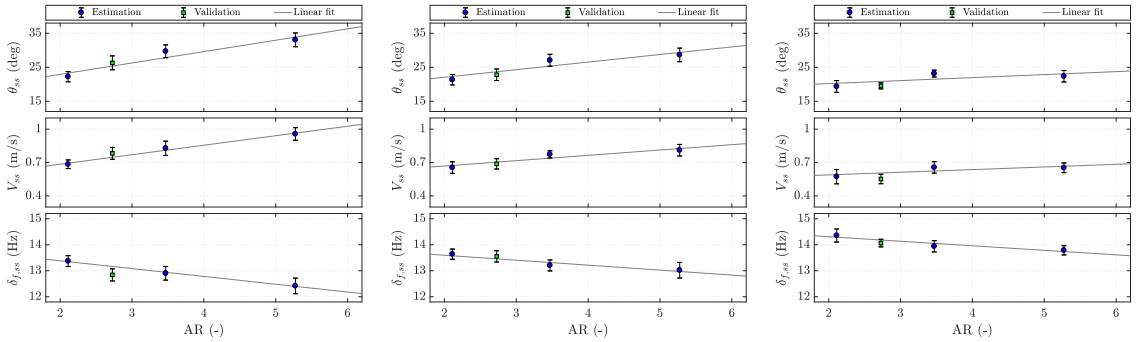

(a) $x_h = 57mm$ (b) $x_h = 98mm$ (c) $x_h = 126mm$

Fig. 9 Steady-state as a function of tail aspect ratio, from free-flight data. 1σ **error-bars.**

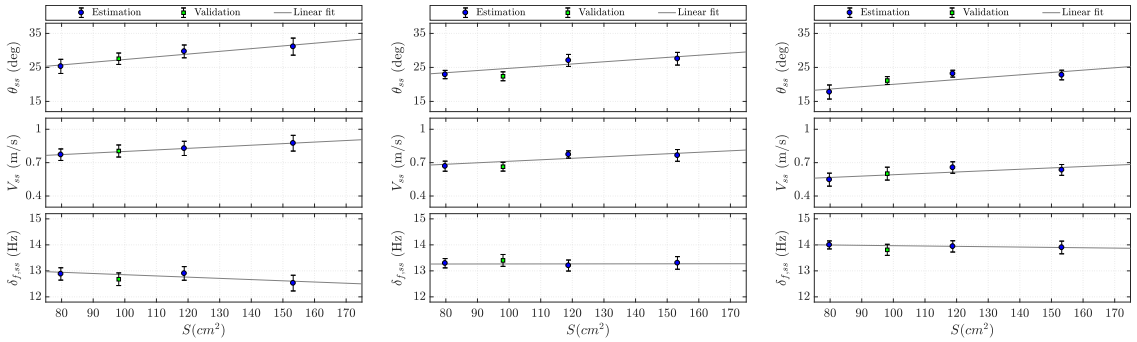

(a) $x_h = 57mm$ (b) $x_h = 98mm$ (c) $x_h = 126mm$

Fig. 10 Steady-state as a function of tail surface area, from free-flight data. 1σ **error-bars.**

Increasing the aspect ratio apparently increases the force generated by the tail and thus causes a larger pitch angle. This in turn tilts the wing force F_w (see Figure 5) and leads to a higher steady-state velocity. It is observed that the effect becomes less pronounced when the tail is moved farther away from the flapping wings, indicated by the less steep slope in the trend in Figure 9(c) in comparison to Figure 9(a).

Increasing the surface area has the same effect on the steady-state as aspect ratio, see Figure 10. However, surface area seems to have a smaller effect on the steady-state conditions than tail AR. Also, the slopes of the linear fits in Figure 10(a) and Figure 10(c) are very similar. This implies that the overall effect of surface area on the steady-state conditions does not vary with longitudinal position.

The steady-state conditions are plotted as a function of the longitudinal position in Figure 11. Increasing the separation from the main wing decreases the steady-state velocity and pitch angle. This is not fully in line with expectations. Moving the tail farther away from the main wing increases the moment arm of the tail force with respect to the CG (see Figure 5), suggesting that the tail would generate more nose-down moment and thus would yield a faster steady-state configuration.

The reason for this result is probably related to the CG shift. Changing the longitudinal position from $x_h = 57mm$ to $x_h = 126mm$ produces an average CG shift of $15.1mm$, depending on the used tail surface, causing a mean increase of the tail moment arm of approximately 74%. However, assuming F_w acting at the wing quarter chord point, the wing moment arm also increases by roughly 40%. According to earlier wind tunnel results the wings actually produce a small, negative contribution in x_b force, thus generating a nose up pitching moment [14, 30]. The steady-state trends observed in Figure 11 imply that the wing contribution is dominant in establishing the moment equilibrium. This can be confirmed by the wind tunnel data in Figure 8, showing that the magnitude of F_x excluding the tail typically reduces by less than 20%. Comparing Figure 11 to Figure 9 and Figure 10 also shows that, overall, the tail geometry has less impact on the steady-state conditions than the longitudinal position of the tail.

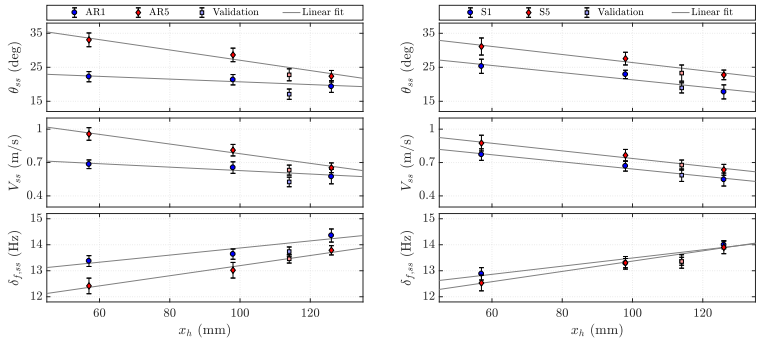

(a) For varying AR (b) For varying S

Fig. 11 Influence of longitudinal position on steady-state conditions. 1σ **error-bars.**

As mentioned before effect of tail position on the steady-state appears the same for configurations S1 and S5, indicated by the near-parallel linear fits in Figure 11(b), but Figure 11(a) shows that the difference in steady-state condition between AR1 and AR5 decreases when x_h increases. It appears that, close to the flapping wings, increasing the AR has more aerodynamic advantage than increasing tail surface area. However, this aerodynamic advantage seems to diminish when moving away from the flapping wings.

At increased x_h the free-stream component is expected to become more dominant over the flapping-wing induced velocity. Since the steady-state attitude is likely determined in part by the total drag of the system this result implies that, for large x_h, the tail is mainly producing a drag force determined mostly by its surface area. Since AR1 and AR5 in Figure 11(a) have the same surface area these ultimately converge to almost the same steady-state conditions when the longitudinal position of the tail increases.

The experiments for configurations AR1d, AR5d, S1d and S5d, e.g., the validation points in Figure 11, were conducted at a later time than the original experiments. Inevitably small changes in the system have taken place during this time, due to the large number of experiments performed. Since the ornithopter is very lightweight and vibrates continuously during flight such changes are inherent to the system and can have a significant impact on the steady-state conditions. This means that an accurate comparison of the steady-state conditions is difficult when measurements are not taken consecutively.

Additional data points were desired to validate if steady-state conditions may be predicted based on tail geometrical parameters. Thus, four additional tail configurations (AR4, AR6, S4, S6) were constructed after the initial experiments. To minimise effects of changes in the system, which can affect steady-state conditions as observed in Figure 11(b), steady-state experiments for $x_h = 57mm$ were repeated in a single day. The results of these experiments are shown in Figure 12. On-board data was not logged during these flights to reduce the required time to do the experiments. This does however mean that motor RPM data is lacking, leading to higher standard deviations in the flapping frequency estimate since it had to be determined solely from OptiTrack data.

Comparing the steady-state conditions in Figure 12(a) to the older ones in Figure 9 confirms that the steady-state conditions can actually vary significantly over time. Especially the results for configuration AR5a ($AR = 5.27$) have significantly changed. However, given that experiments are performed in succession, with minimal changes made to the system in between, it is in fact possible to accurately predict steady-state conditions as a simple, linear function of tail aspect ratio or surface area. The trends in Figure 12 are also the same as those found during earlier experiments (Figure 9 and Figure 10), and thus the observed effects of the tail geometry on the steady-state conditions are considered valid.

The prediction errors are summarised in Table 3, showing that the predictions are less than one standard deviation from the measurements. It is even possible to extrapolate the trends a little beyond the original estimation range and still predict the steady-state conditions with good accuracy. This provides interesting opportunities for future design tools.

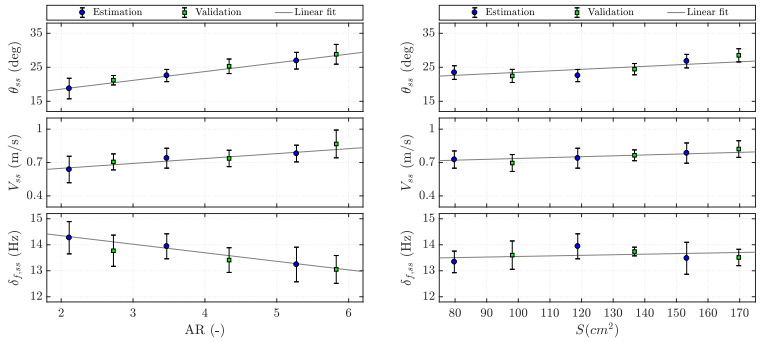

(a) Function of tail AR. (b) Function of tail S.

Fig. 12 New steady-state experiments performed to validate if steady-state conditions can be accurately predicted based on tail geometry. $\mathbf{x_h = 57mm}$. 1σ error-bars.

Table 3 Result of predicting steady-state conditions, for results in Figure 12, using linear fits.

	$\theta_{ss}(deg)$				$V_{ss}(ms^{-1})$				$\delta_{f,ss}(Hz)$			
Tail	x_m	$\hat{x}$	$\lvert x_m - \hat{x}\rvert$	$\lvert\frac{x_m-\hat{x}}{\sigma(x)}\rvert$	x_m	$\hat{x}$	$\lvert x_m - \hat{x}\rvert$	$\lvert\frac{x_m-\hat{x}}{\sigma(x)}\rvert$	x_m	$\hat{x}$	$\lvert x_m - \hat{x}\rvert$	$\lvert\frac{x_m-\hat{x}}{\sigma(x)}\rvert$
AR2a	21.20	20.48	0.74	0.54	0.71	0.67	0.03	0.36	13.77	14.11	0.34	0.57
AR4a	25.30	24.61	0.69	0.32	0.74	0.75	0.01	0.19	13.41	13.58	0.17	0.36
AR6a	28.83	28.45	0.37	0.13	0.87	0.82	0.05	0.40	13.05	13.09	0.04	0.07
S2a	22.46	23.43	0.97	0.50	0.70	0.74	0.04	0.21	13.60	13.54	0.06	0.10
S4a	24.45	25.14	0.69	0.42	0.76	0.77	0.01	0.29	13.74	13.63	0.11	0.66
S6a	28.53	26.60	1.93	1.00	0.82	0.79	0.03	0.06	13.51	13.70	0.19	0.61

2. Effect on dynamic behaviour

During free-flight experiments, differences in response were clearly visible for the different configurations. Analysing the time response of each configuration should thus provide valuable insights into the effect of the tail.

Figure 13 shows average time responses for varying AR. The average response is computed over all the manoeuvres performed during an experiment. The results show that an increased aspect ratio has a positive effect on damping capabilities and also slightly reduces the natural frequency of the oscillation. This might be partially caused by the increased span width of AR3 and AR5. This gives these configurations effective tail area in a span-wise region which experiences a high induced velocity wake, according to PIV measurements and numerical studies performed for this ornithopter (cf. Fig. 9 in [22] or Fig. 14 in [20]). Note that apparent differences in input in Figure 13 and other time response figures are caused by tracking problems of the elevator marker and subsequent averaging over multiple data segments.

The results in Figure 13 also show that the responses vary greatly with changing longitudinal position of the tail. When the distance to the flapping wings is small, Figure 13(a), increasing the aspect ratio seems to have a little more effect on the natural frequency of the oscillation but the responses are in fact quite similar. In Figure 13(b) the differences in average response are far more evident and clearly show increased damping for configurations AR3d and AR5d. Though the initial responses are almost identical, the peak at $t \approx 1.4s$ decreases considerably in magnitude for high AR configurations. These differences in damping are also apparent in Figure 13(c). In fact, increasing x_h beyond $114mm$ appears to drastically reduce the damping capabilities of configuration AR1c, and to lesser extent for AR2c, but it does not for AR3c and AR5c.

Figure 14 shows the average time responses for tails of different surface area. Differences in damping again become more apparent for increased longitudinal position of the tail, see Figure 14(c). From Figure 14(a) it seems that increasing the surface area beyond $S = 153.3cm^2$, i.e., from S5a to S6a, does not produce any significant change in dynamic response.

Increased surface area seems to have some effect on the natural frequency of the oscillation when the tail is close to the flapping wings, based on the time responses of in Figure 14(a), though

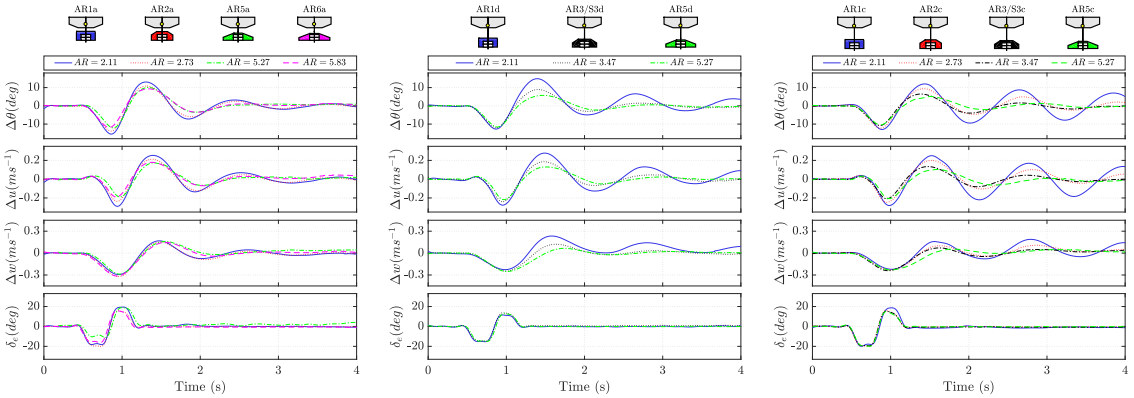

(a) $x_h = 57mm$ (b) $x_h = 114mm$ (c) $x_h = 126mm$

Fig. 13 Influence of tail aspect ratio on average time response to elevator doublet.

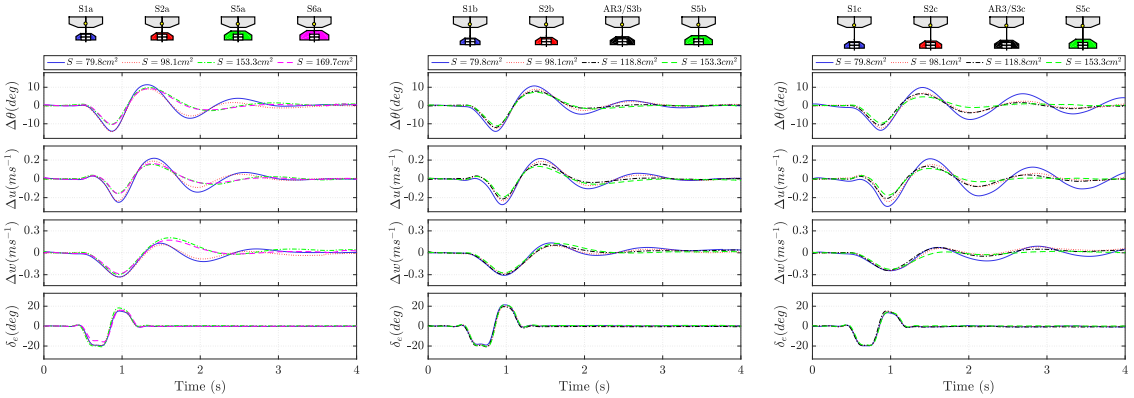

(a) $x_h = 57mm$ (b) $x_h = 98mm$ (c) $x_h = 126mm$

Fig. 14 Influence of tail surface area on average time response to elevator doublet.

the oscillations in Figure 14(c) are almost perfectly in-phase, showing only differences in damping. Damping is reduced for S1c in comparison to S1b. This is unexpected, since the tail moment arm increases from $x_h = 98mm$ to $x_h = 126mm$. Similar to the results for the steady-state conditions in Figure 11, this may be a result of the wing force also generating a larger, destabilising moment when the CG is moved further aft.

From Figure 13 and Figure 14 it is apparent that the longitudinal position of the tail has significant impact on the dynamic behaviour of the ornithopter for a given tail geometry. This is visualised more clearly in Figure 15, which shows results for tail configurations at varying longitudinal position.

Figure 15(c) shows that damping increases up to $x_h = 98mm$ but decreases significantly when the tail position is increased beyond that for configuration AR1. The same is observed for configuration S1, Figure 15(a), though the difference is smaller than for AR1. In contrast, Figure 15(b) shows that damping of the oscillation remains high even up to $x_h = 126mm$ for configuration AR3/S3. Increasing the distance between the tail and the flapping wings is actually expected to improve damping, as the moment arm of the tail force increases (see Figure 5). Given that configuration S3/AR3 matches the aspect ratio of configuration S1 and the surface area of configuration AR1, the decrease in damping at high x_h, for configurations AR1c and S1c, cannot be linked directly to either surface area or aspect ratio of the tail surface.

It is expected that the maximum span width of the tails plays a role in the explanation of this result. Configurations S1 and AR1 feature relatively small span widths of 158 and $166mm$ respectively. Configuration S3 has a larger span width of $203mm$. The results observed in Figure 15 could be explained by the typical induced velocity profile of flapping wings, which experiences peaks at $60 - 70\%$ of the flapping wing span [22, 36]. Energy in the wake of the flapping wings dissipates

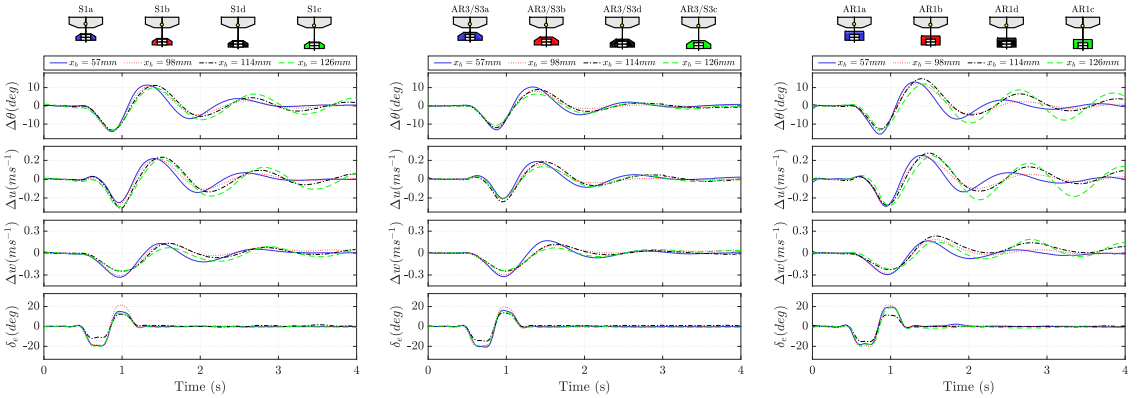

(a) S1 ($S = 79.8cm^2,\ AR = 3.45$)

(b) AR3/S3 ($S = 118.8cm^2,\ AR = 3.47$)

(c) AR1 ($S = 118.2cm^2,\ AR = 2.11$)

Fig. 15 Influence of longitudinal position on average time response to elevator doublet.

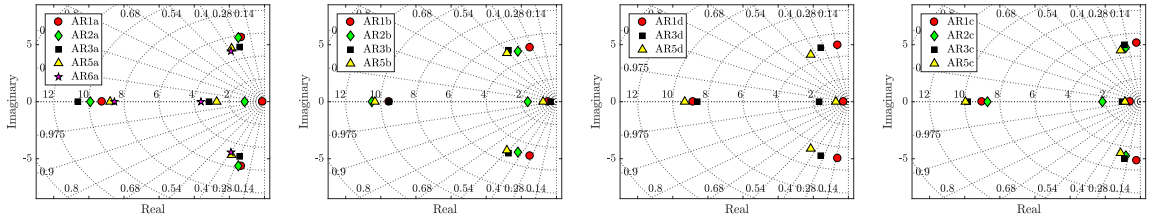

(a) $x_h = 57mm$

(b) $x_h = 98mm$

(c) $x_h = 114mm$

(d) $x_h = 126mm$

Fig. 16 Pole plots illustrating effect of tail aspect ratio on the system eigenvalues.

when moving downstream in chord-wise direction, decreasing the magnitude of the induced velocity. The region of high induced velocity is also found to decrease in span-wise direction when moving further away from the flapping wings, resembling a bell shape (cf. Fig. 8 in [22]). In light of this, tails with a smaller span width are likely not seeing this high induced velocity field anymore when x_h is large, thus drastically reducing their effectiveness when the longitudinal position exceeds $98mm$.

The time responses indicate changes in damping and natural frequency of the oscillatory eigenmode of the ornithopter, which can be further studied by analysing the eigenvalues of the estimated models. Figure 16 shows the results for varying tail aspect ratio. The plots illustrate the eigenvalues of the most representative averaged model for each configuration, based on the validation results (see Table A.2). There is a clear trend in the complex conjugate pair of eigenvalues but the real eigenvalues show less consistent trends. As mentioned earlier, the real eigenvalues for individual models generally are less consistent than the complex conjugate eigenvalues (see Figure 7(b)), though it is clear that the ornithopter has two aperiodic eigenmodes with eigenvalues at approximately -1 and -10. The inconsistency in the aperiodic eigenvalues was also encountered in previous system identification work and is likely caused by insufficient excitation of the dynamics associated with these eigenvalues, i.e., the dynamics in the body z_b-axis [13].

In line with the time response results in Figure 13, increasing the tail AR slightly reduces the natural frequency of the response and has some positive effect on damping for $x_h = 57mm$, Figure 16(a). For $x_h = 114mm$ and higher, Figure 16(c) and Figure 16(d), increasing the AR leads to significant improvements in damping of the oscillation but hardly has an effect on the natural frequency.

Figure 17 shows the pole-zero plots for varying tail surface area. The results are similar to those seen for changing the AR and are again in line with what is observed in the average time responses in Figure 14. The complex conjugate eigenvalues for the two largest tail configurations, S5a and S6a in Figure 17(a) are in fact very similar which corresponds to the marginal difference in time response observed in Figure 14(a).

Figure 17(b) shows that for $x_h = 98mm$ an increase in surface area already mostly has an

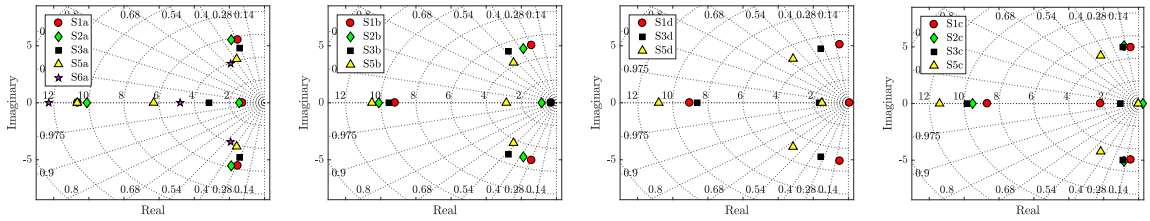

(a) $x_h = 57mm$ (b) $x_h = 98mm$ (c) $x_h = 114mm$ (d) $x_h = 126mm$

Fig. 17 Pole plots illustrating effect of tail surface area on the system eigenvalues.

Table 4 Estimated stability derivatives and standard deviations for varying S, $x_h = 98mm$.

	S1b		S2b		S3b		S5b	
	$\hat{\theta}$	$100\lvert\hat{\sigma}/\hat{\theta}\rvert$	$\hat{\theta}$	$100\lvert\hat{\sigma}/\hat{\theta}\rvert$	$\hat{\theta}$	$100\lvert\hat{\sigma}/\hat{\theta}\rvert$	$\hat{\theta}$	$100\lvert\hat{\sigma}/\hat{\theta}\rvert$
M_q	-4.41e-04	0.48	-6.46e-04	0.57	-7.30e-04	0.49	-9.03e-04	0.54
M_u	-1.90e-03	0.45	-1.79e-03	0.64	-2.06e-03	0.67	-1.70e-03	0.66
M_w	-3.76e-05	23.30	-7.91e-04	2.05	-6.59e-04	1.56	-1.27e-03	0.82
X_q	1.89e-02	0.77	1.85e-02	1.05	2.93e-02	0.47	3.15e-02	0.50
X_u	-1.30e-01	0.56	-1.26e-01	0.45	-1.34e-01	0.34	-1.43e-01	0.23
X_w	-1.13e-02	6.06	-4.13e-02	1.57	-2.12e-02	1.56	-3.06e-02	0.98
Z_q	-1.26e-03	19.63	1.79e-03	24.20	1.36e-03	29.17	-2.22e-03	11.04
Z_u	1.84e-02	4.56	1.78e-02	5.96	-7.86e-04	123.50	1.58e-02	3.67
Z_w	-1.07e-02	4.16	-9.43e-03	8.10	2.05e-03	23.80	-1.79e-02	2.71

effect on damping, while there is quite a significant effect on the natural frequency of the response for $x_h = 57mm$ in Figure 17(a). For $x_h = 126mm$, in Figure 17(d), increasing the surface area mostly results in an increase in damping. The results imply that the behaviour of the system changes significantly for longitudinal tail positions between $98 - 114mm$. Configurations S1 and S3 lose considerable damping capabilities between these two fuselage lengths, as can be seen from Figure 17(b) and Figure 17(c). This is most likely related to the strength of the wake induced by the flapping wings and may be related to the free-stream velocity becoming dominant over flapping-wing induced velocity at increased distance from the flapping wings. In that case the horizontal tail most likely acts as a flat plate translating at high angle of attack, causing significant decreases in aerodynamic force generation [28].

Wake modelling for this ornithopter, in hover conditions, in a recent study by Armanini et al. ([22]) confirms that the induced velocity indeed decreases significantly with increased distance from the flapping wings. In this study the flow conditions at the tail are modelled by simple addition of the induced flow in hover to free-stream velocities encountered in free-flight. Future work should perform wake modelling in real slow forward flight conditions, using a wind tunnel for example, to investigate the actual interaction between free-stream flow and flapping-wing induced flow. This should help determine at which distance from the flapping wings the free-stream component in fact starts to become dominant.

The ability to design configurations with specific dynamic properties based on tail geometry, using simple models, would be a great benefit for FWMAV development. As an example, Table 4 shows the estimated stability derivatives for varying surface area and the estimated standard deviations. These are the model parameters of the most representative average models, which for all of these configurations was the TA model. The parameter values in Table 4 are in the same order of magnitude as those found in previous system identification efforts performed for this FWMAV [27]. From the estimated standard deviations in Table 4 it is clear that most parameters are estimated quite successfully. Parameters coupled to the body z_b-axis do show high estimated standard deviations, which is likely caused by a lack of excitation in this direction and seems to correspond to the less consistent real eigenvalues seen in Figure 17. The same lack of excitation is suspected to cause the high estimated standard deviations for M_w, X_w and Z_w.

Table 4 does not immediately reveal very clear trends in the model parameters with changing

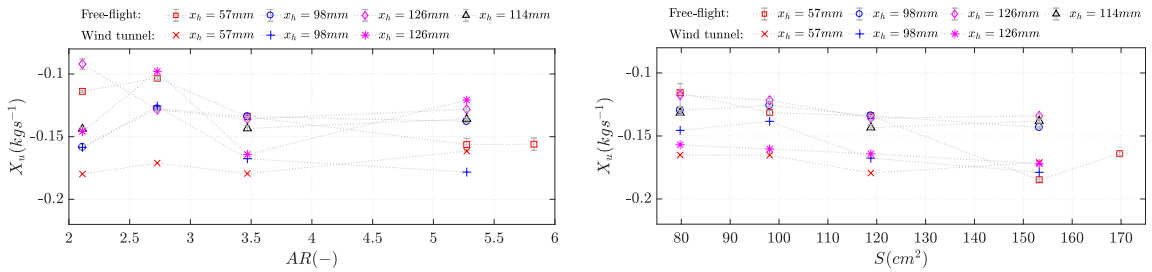

(a) As function of AR.

(b) As function of surface area.

Fig. 18 Effect of tail geometry on X_u, estimated from free-flight and wind tunnel data.

surface area. In general, identifying trends in the model parameters based on tail geometry proved to be very difficult using the current modelling efforts. The results for two parameters which are important in determining dynamic stability, X_u and M_q, are shown in Figure 18 and Figure 19. Only the parameter values of the most representative model for each configuration are presented here.

X_u is a measure of the drag force as a result of changes in forward velocity. It is expected that the drag is influenced by the geometry of the tail, in particular surface area. Based on the results in Figure 18, X_u indeed shows a stronger trend with surface area than with aspect ratio. X_u seems fairly constant with differing aspect ratio according to the data in Figure 18(a). Figure 18(b) shows a slightly more distinct trend, with an increasing magnitude of X_u for higher surface area. This is in line with expectations, since a higher surface area translating through air generally leads to a higher drag force. The wind tunnel results also show a slight trend with tail surface area, Figure 18(b), but vary quite a bit from the free-flight results in magnitude. Actually comparing these stability derivatives would require more study into the accuracy of both experimental methods (see also Caetano et al. [31]). Ultimately, the results in Figure 18(b) do not show very conclusive trends and it was not considered feasible to develop a model for X_u as a function of tail surface area.

M_q is an important stability parameter determining the corrective moment generated in case of a pitch disturbance. For dynamic stability its sign should be negative. Figure 19 shows the results as a function of tail geometry. Again, surface area appears to have more effect, though a trend is also visible for increasing aspect ratio, Figure 19(a). Increasing AR or surface area leads to an increase in magnitude of M_q. This is in line with the observations that increasing tail surface area or AR has a positive effect on damping (see Figure 16 and Figure 17). Also in line with previous observations, surface area has more effect on the damping capabilities of the tail surface than aspect ratio, illustrated by the larger increase in magnitude of M_q in Figure 18(b), especially for configuration S5 ($S = 153.3cm^2$).

From Figure 19 it is also observed that M_q is not significantly influenced by the longitudinal position of the tail. This suggests that changes in damping for a specific tail at different longitudinal positions x_h may result more from an increase in inertia (I_{yy}) than due to changes in the aerodynamic effect of the tail. Increasing the longitudinal position of the tail from $x_h = 57mm$ to $x_h = 126mm$ actually increases I_{yy} by an average 150%, due to mass moving further away from the CG. The results in Figure 19 indicate that the aerodynamic damping capabilities of most tail geometries increases up to $x_h = 98mm$. When the distance between the tail and the flapping wings is increased even further, inertia effects become dominant.

The results in Figure 19 do suggest that increasing AR and/or surface area increases F_h, which in turn leads to a larger stabilising moment generated by the tail (also refer back to Figure 5). On top of that, the added mass force may also play a role here. As the ornithopter experiences acceleration it is subjected to a reaction force of the accelerated fluid surrounding it. This is often modelled using a quasi-steady approach with a time-invariant added mass coefficient [5]. During manoeuvres the FWMAV experiences very high angular accelerations about the body y_b axis. Armanini et al. model the added mass of the wing as that of a flat plate, being a quadratic function of local chord length (c^2) integrated along the span-wise direction [14]. Assuming the same relation for the tail surface could help explain the larger variation in M_q for increasing surface area, as these tails feature larger variation in chord length (refer to Table A.1).

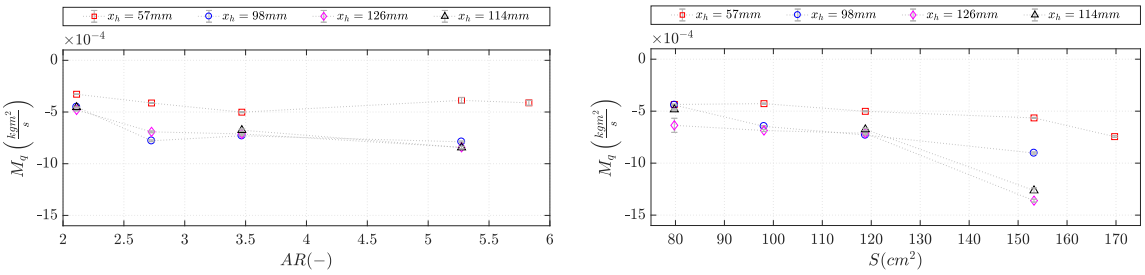

(a) As function of AR. (b) As function of S.

Fig. 19 Effect of tail geometry on M_q, from free-flight data.

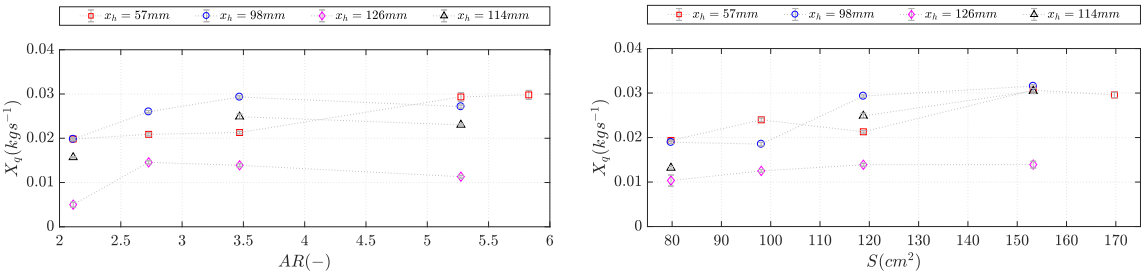

(a) As function of AR. (b) As function of S.

Fig. 20 Effect of tail geometry on X_q, from free-flight data.

The cross-coupling terms M_u and X_q are also important parameters in terms of the oscillatory response of the system. Results from free-flight are given in Figure 20 and Figure 21. Increasing the tail aspect ratio or the surface area leads to a slight increase in X_q. This corresponds to an improvement of the damping capabilities. Figure 20 also shows an influence of the longitudinal position on the magnitude of X_q, though there is no clear trend. It appears that X_q increases in magnitude with increasing longitudinal position at first (up to $x_h = 98mm$) and then decreases again for $x_h = 114mm$ and higher, especially clear in the results for $AR = 3.47$ in Figure 20(a).

The results in Figure 21 do not show any significant effects of the tail geometry on the magnitude of M_u. There is however a rather clear trend with the longitudinal position of the tail. The results indicate that coupling between the velocity in body x_b-axis and the pitching moment increases when the tail is moved further away from the flapping wings. This is as would be expected since increasing x_h increases the moment arms of both the wings and the tail surface. The negative sign of M_u indicates that an increase in body velocity u leads to a negative, i.e., pitch up, moment change. This, and the fact that M_u does not change significantly with tail geometry, according to the results in Figure 21, implies that the wing force is dominant in contributing to M_u.

In general the averaged models, for a given configuration, showed quite large variations in model

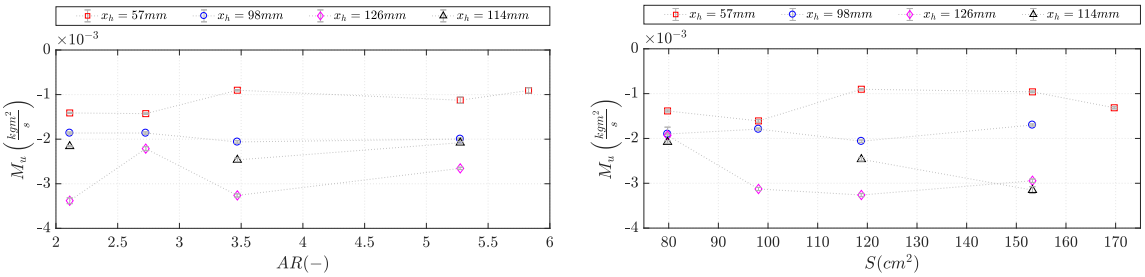

(a) As function of AR. (b) As function of S.

Fig. 21 Effect of tail geometry on M_u, from free-flight data.

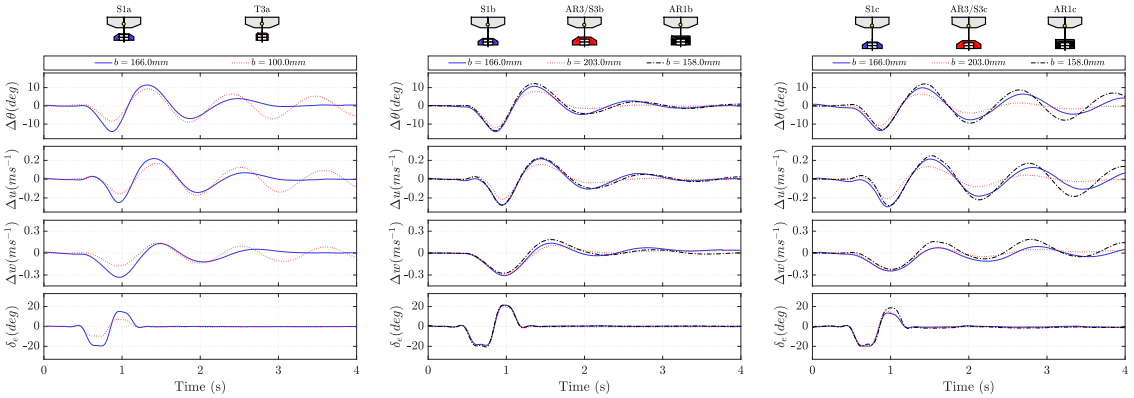

(a) $x_h = 57mm$ (b) $x_h = 98mm$ (c) $x_h = 126mm$

Fig. 22 Effect of tail span width on average time response.

parameters even though the resulting predicted behaviour was similar, especially for the oscillatory component. This suggests that some model parameters, such as Z_u and X_w, have little effect on the pitch dynamics. The results in Table 4 confirm this, as the relatively high standard deviations of these parameters seemingly do not have a significant impact on the performance of the models. For a better understanding of the model parameters and their specific effect on the final model performance it is suggested to perform a systematic sensitivity analysis of the LTI model parameters in future work. Fixing some of the less important parameters might improve the accuracy of the overall model and decrease the variability of the important parameters such as M_q.

3. Effect of tail span width

From the results in Figure 15 the hypothesis arose that the maximum span width of the horizontal tail plays a role in the dynamic behaviour of the ornithopter. The behaviour of tail configurations with the same AR and surface area seems to vary significantly when the distance between the tail and the flapping wings is large. To illustrate, Figure 22 shows time response results for several tails as a function of their maximum span width.

Most notable is the large difference in response between configurations T3a and S1a in Figure 22(a). Configuration T3a starts oscillating heavily about its steady-state even with a smaller elevator input, while tail S1a is damped fairly well. Configurations T3b and T3c even tended to be destabilised by 30% elevator deflections, making it impossible to accurately estimate LTI models for these configurations. The difference in behaviour seen in Figure 22(a) is more extreme than expected from the difference in surface area and aspect ratio alone, based on the results in Figure 13 and Figure 14. It is expected that the increased span width of configuration S1a may contribute to this significant increase in damping capabilities, since the induced velocity in the in-board region, close to the root of the flapping wings, decreases significantly [20, 22, 36].

The results in Figure 22(b) and Figure 22(c) support this hypothesis. These figures show results for two configurations with similar maximum span width (S1 and AR1) and one configuration with a larger span width (AR3/S3), at two different longitudinal positions x_h. Despite differences of 63.6% and 48.2% in AR and surface area, respectively, between configurations S1 and AR1, the responses of these configurations are very similar, especially in terms of damping. Configuration AR3c, Figure 22(c), which has a larger maximum span width, shows much better damping capabilities even though it has the same aspect ratio as configuration S1 and the same surface area as configuration AR1. The aerodynamic importance of maximum span width has previously been noted by Thomas in his study of bird tail aerodynamics [18]. The results in Figure 22 seem to support this.

Since AR, surface area and span width are all related through the relation for aspect ratio (Equation (1)) it is impossible to isolate the contribution of one of these parameters to the dynamic behaviour without changing at least one of the other variables. Therefore additional research is needed to give definitive conclusions about the relevance of the maximum span width. It is recommended to extend previous studies, modelling the wake of the flapping wings of this ornithopter

in hover conditions by means of PIV measurements ([22]), to slow forward flight conditions. This should give more insight into the flow conditions at the tail, especially in span-wise direction, and may help to quantify the effect of the span width of the tail surface on its total effectiveness.

V. Conclusion

This paper presented the results of a systematic study into the effect of the horizontal tail on the time-averaged dynamics of a flapping-wing micro aerial vehicle, the DelFly II. Three parameters were varied to investigate their effect: surface area, aspect ratio and longitudinal position.

It was found that increased surface area and aspect ratio provides a larger pitch down moment, tipping the moment equilibrium and thus increasing steady-state velocity. It can be concluded that the tail force increases in magnitude with increased S and AR. Using additional test configurations it was shown that prediction of the steady-state conditions based on tail geometry is possible with simple linear relations. This provides interesting opportunities for future FWMAV platform design tools.

Increasing the longitudinal position of the tail decreases the steady-state velocity. This is most likely caused by the shift in CG position. Based on the results, forces generated by the wing are dominant in determining the moment equilibrium and therefore the increased moment arm of the wing results in slower flight. Results also suggest that the effectiveness of the tail decreases with increased distance to the flapping wings, possibly due to less energy being available in the wake.

Increasing aspect ratio and surface area generally increases damping of the periodic, oscillatory eigenmode and slightly decreases natural frequency. For increased distance to the flapping wings the effect on natural frequency becomes less but significant changes in damping were observed. Some tail geometries experienced a significant decrease in damping capabilities at longitudinal positions exceeding $98mm$. This appears connected to the maximum span width of the tail surface rather than just its surface area or aspect ratio. More research into the effect of maximum tail span width is recommended.

Trends were identified in some stability derivatives, mainly M_q, X_q, M_u and X_u. However, the current models did not reveal trends with enough confidence to predict dynamic behaviour based on tail geometry. Future studies may focus more on the system identification cycle to improve model accuracy, for example with a thorough sensitivity study of the model parameters. It is also recommended to further investigate the possibility of increasing model accuracy using throttle input data, as this provides better excitation in the body z_b axis than elevator inputs.

In the context of novel FWMAV platform designs, it is suggested to systematically study the effect of a non-zero angle of the horizontal tail with respect to the fuselage. Some birds tilt their tails for flight control purposes and it should be interesting to study the potential benefits of such a feature for robotic flappers. Future research may also focus on the vertical tail surface and its effects on the lateral dynamics of the ornithopter.

Appendix

Table A.1 Physical dimensions of the tail geometries used in the experiments.

	Tail identifier													
Parameter	S1	S2	S3/AR3	S4	S5	S6	AR1	AR2	AR4	AR5	AR6	T1	T2	T3
b (mm)	166	184	203	217	230	242	158	180	227	250	260	170	170	100
b_{LE} (mm)	87	96	105	112	120	126	152	90	80	70	76	80	-	70
c_r (mm)	54	60	66	71	75	79	75	73	64	60	57	71	73	60
c_t (mm)	29	32	35	38	40	42	66	45	28	25	22	38	24	50
AR $(-)$	3.45	3.45	3.47	3.44	3.45	3.45	2.11	2.73	4.34	5.27	5.83	2.73	2.72	1.71
S (cm^2)	79.8	98.1	118.8	136.7	153.3	169.7	118.2	118.8	118.82	118.5	116.0	105.9	106.2	58.5

Table A.2 Mean validation scores, standard deviation in brackets. Not all configurations were tested. For T3b and T3c, modelling was unsuccessful.

		Fuselage configuration							
		a ($x_h = 57mm$)		b ($x_h = 98mm$)		c ($x_h = 126mm$)		d ($x_h = 114mm$)	
Tail	Model	RMS	PCC	RMS	PCC	RMS	PCC	RMS	PCC
S1	TA	0.12 (0.02)	0.88 (0.03)	0.11 (0.01)	0.87 (0.05)	0.10 (0.01)	0.86 (0.02)	0.11 (0.02)	0.84 (0.05)
	WM	0.12 (0.02)	0.87 (0.02)	0.16 (0.02)	0.64 (0.11)	0.11 (0.01)	0.85 (0.05)	0.13 (0.01)	0.84 (0.04)
	Mean	0.12 (0.01)	0.86 (0.05)	0.11 (0.01)	0.83 (0.06)	0.09 (0.01)	0.88 (0.05)	0.13 (0.03)	0.77 (0.11)
S2	TA	0.10 (0.02)	0.84 (0.09)	0.11 (0.02)	0.86 (0.05)	0.10 (0.01)	0.83 (0.09)	-	-
	WM	0.12 (0.02)	0.72 (0.12)	0.14 (0.01)	0.78 (0.05)	0.20 (0.03)	0.63 (0.13)	-	-
	Mean	0.10 (0.02)	0.81 (0.11)	0.12 (0.01)	0.80 (0.05)	0.10 (0.02)	0.79 (0.04)	-	-
S3/AR3	TA	0.12 (0.02)	0.78 (0.08)	0.09 (0.01)	0.87 (0.03)	0.10 (0.01)	0.80 (0.06)	0.09 (0.01)	0.90 (0.06)
	WM	0.17 (0.02)	0.62 (0.14)	0.10 (0.02)	0.81 (0.07)	0.11 (0.01)	0.75 (0.06)	0.13 (0.02)	0.73 (0.12)
	Mean	0.12 (0.02)	0.75 (0.07)	0.10 (0.01)	0.86 (0.03)	0.10 (0.01)	0.79 (0.05)	0.09 (0.01)	0.90 (0.05)
S5	TA	0.09 (0.04)	0.86 (0.07)	0.08 (0.02)	0.88 (0.03)	0.09 (0.02)	0.79 (0.04)	0.11 (0.03)	0.80 (0.08)
	WM	0.11 (0.04)	0.82 (0.06)	0.11 (0.01)	0.76 (0.05)	0.12 (0.02)	0.59 (0.07)	0.16 (0.02)	0.48 (0.09)
	Mean	0.09 (0.04)	0.85 (0.07)	0.09 (0.02)	0.84 (0.04)	0.10 (0.02)	0.71 (0.07)	0.12 (0.02)	0.76 (0.11)
S6	TA	0.09 (0.03)	0.89 (0.05)	-	-	-	-	-	-
	WM	0.11 (0.02)	0.85 (0.05)	-	-	-	-	-	-
	Mean	0.09 (0.03)	0.89 (0.05)	-	-	-	-	-	-
AR1	TA	0.14 (0.05)	0.78 (0.27)	0.12 (0.02)	0.86 (0.01)	0.13 (0.01)	0.86 (0.04)	0.14 (0.02)	0.84 (0.06)
	WM	0.15 (0.04)	0.73 (0.24)	0.18 (0.01)	0.59 (0.06)	0.16 (0.05)	0.78 (0.13)	0.13 (0.04)	0.84 (0.07)
	Mean	0.14 (0.05)	0.75 (0.29)	0.12 (0.02)	0.83 (0.03)	0.18 (0.02)	0.75 (0.07)	0.14 (0.03)	0.81 (0.11)
AR2	TA	0.10 (0.04)	0.89 (0.05)	0.11 (0.03)	0.87 (0.07)	0.08 (0.02)	0.89 (0.04)	-	-
	WM	0.13 (0.03)	0.80 (0.06)	0.12 (0.03)	0.82 (0.09)	0.09 (0.02)	0.85 (0.05)	-	-
	Mean	0.10 (0.03)	0.87 (0.05)	0.11 (0.03)	0.85 (0.06)	0.08 (0.02)	0.88 (0.04)	-	-
AR5	TA	0.12 (0.03)	0.85 (0.05)	0.10 (0.02)	0.83 (0.08)	0.11 (0.01)	0.70 (0.15)	0.12 (0.03)	0.82 (0.02)
	WM	0.18 (0.03)	0.72 (0.07)	0.12 (0.01)	0.75 (0.07)	0.13 (0.01)	0.53 (0.07)	0.13 (0.03)	0.76 (0.08)
	Mean	0.10 (0.03)	0.86 (0.06)	0.10 (0.03)	0.78 (0.09)	0.11 (0.01)	0.65 (0.19)	0.13 (0.04)	0.73 (0.11)
AR6	TA	0.11 (0.02)	0.85 (0.05)	-	-	-	-	-	-
	WM	0.12 (0.02)	0.80 (0.07)	-	-	-	-	-	-
	Mean	0.10 (0.02)	0.87 (0.06)	-	-	-	-	-	-
T1	TA	0.11 (0.03)	0.88 (0.06)	0.10 (0.03)	0.88 (0.05)	0.14 (0.03)	0.76 (0.07)	-	-
	WM	0.75 (0.65)	0.44 (0.23)	0.15 (0.04)	0.74 (0.10)	0.29 (0.09)	0.32 (0.28)	-	-
	Mean	0.11 (0.03)	0.87 (0.04)	0.10 (0.03)	0.87 (0.06)	0.13 (0.04)	0.76 (0.10)	-	-
T2	TA	0.10 (0.01)	0.86 (0.03)	0.11 (0.05)	0.90 (0.06)	0.67 (0.61)	0.47 (0.30)	-	-
	WM	0.17 (0.03)	0.75 (0.07)	0.15 (0.03)	0.75 (0.11)	0.19 (0.03)	0.68 (0.18)	-	-
	Mean	0.12 (0.01)	0.83 (0.04)	0.13 (0.05)	0.82 (0.08)	0.17 (0.03)	0.67 (0.16)	-	-
T3	TA	0.29 (0.13)	0.87 (0.12)	-	-	-	-	-	-
	WM	1.16 (0.85)	0.44 (0.21)	-	-	-	-	-	-
	Mean	0.34 (0.10)	0.67 (0.09)	-	-	-	-	-	-

References

[1] Dickinson, M., Lehmann, F., and Sane, S., "Wing Rotation and the Aerodynamic Basis of Insect Flight," *Science*, Vol. 284, 1999, pp. 1954–1960.

[2] Ellington, C., "The Aerodynamics of Hovering Insect Flight. I. The Quasi-Steady Analysis," *Philosophical Transactions of the Royal Society of London, Series B: Biological Sciences*, Vol. 305, 1984, pp. 1–15.

[3] Chin, D. and Lentink, D., "Flapping wing aerodynamics: from insect to vertebrates," *Journal of Experimental Biology*, Vol. 219, 2016, pp. 920–932.

[4] Sane, S. and Dickinson, M., "The aerodynamic effects of wing rotation and a revised quasi-steady model of flapping flight," *Journal of Experimental Biology*, Vol. 205, 2002, pp. 1087–1096.

[5] Sane, S. P., "The aerodynamics of insect flight," *Journal of Experimental Biology*, Vol. 206, 2003, pp. 4191–4208.

[6] Birch, J. and Dickinson, M., "The influence of wing-wake interactions on the production of aerodynamic force in flapping flight," *Journal of Experimental Biology*, Vol. 206, 2003, pp. 2257–2272.

[7] de Croon, G., Groen, M., de Wagter, C., Remes, B., Ruijsink, R., and van Oudheusden, B., "Design, aerodynamics and autonomy of the DelFly," *Bioinspiration & Biomimetics*, Vol. 7, No. 2, 2012, pp. 1–16.

[8] Grauer, J., Ulrich, E., Hubbard, J., Pines, D., and Humbert, J., "Testing and System Identification of an Ornithopter in Longitudinal Flight," *Journal of Aircraft*, Vol. 48, No. 2, 2011, pp. 660–667.

[9] Rosen, M., le Pivain, G., Sahai, R., Jafferis, N., and Wood, R., "Development of a 3.2g Untethered Flapping-Wing Platform for Flight Energetics and Control Experiments," in "2016 IEEE International Conference on Robotics and Automation (ICRA)," Stockholm, Sweden, 2016, pp. 3227–3233.

[10] Ma, K., Chirarattananon, P., Fuller, S., and Wood, R., "Controlled Flight of a Biologically Inspired, Insect-Scale Robot," *Science*, Vol. 340, 2013, pp. 603–607.

[11] Keennon, M., Klingebiel, K., Won, H., and Andriukov, A., "Development of the Nano Hummingbird: A Tailless Flapping Wing Micro Air Vehicle," in "50th AIAA Aerospace Sciences Meeting including the New Horizons Forum and Aerospace Exposition," Nashville, Tennessee, 2012.

[12] Caetano, J., de Visser, C., de Croon, G., Remes, B., de Wagter, C., Verboom, J., and Mulder, M., "Linear Aerodynamic Model Identification of a Flapping Wing MAV Based on Flight Test Data," *International Journal of Micro Air Vehicles*, Vol. 5, 2013, pp. 273–286.

[13] Armanini, S., Karásek, M., de Visser, C., de Croon, G., and Mulder, M., "Flight testing and preliminary analysis for global system identification of ornithopter dynamics using on-board and off-board data," in "AIAA Atmospheric Flight Mechanics Conference," Grapevine, Texas, 2017.

[14] Armanini, S., Caetano, J., de Croon, G., de Visser, C., and Mulder, M., "Quasi-Steady Aerodynamic Model of Clap-and-Fling Flapping MAV and Validation using Free-Flight Data," *Bioinspiration & Biomimetics*, Vol. 11, No. 4.

[15] Groen, M., Bruggeman, B., Remes, B., Ruijsink, R., van Oudheusden, B., and Bijl, H., "Improving flight performance of the flapping wing MAV DelFly II," in "International Micro Air Vehicle conference and competitions (IMAV 2010)," , 2010.

[16] de Croon, G., de Clerq, K., Ruijsink, R., Remes, B., and de Wagter, C., "Design, aerodynamics, and vision-based control of the DelFly," *International Journal of Micro Air Vehicles*, Vol. 1, No. 2, 2009, pp. 71–97.

[17] Wood, R., "The First Takeoff of a Biologically Inspired At-Scale Robotic Insect," *IEEE Transactions on Robotics*, Vol. 24, No. 2, 2008, pp. 341–347.

[18] Thomas, A., "On the aerodynamics of birds' tails," *Philos. Trans. R. Soc. London, Ser. B*, Vol. 340, 1993, pp. 361–380.

[19] de Croon, G., Percin, M., Remes, B., Ruijsink, R., and de Wagter, C., *The DelFly: Design, Aerodynamics, and Artificial Intelligence of a flapping Wing Robot*, Springer, 2016.

[20] Tay, W., Bijl, H., and van Oudheusden, B., "Biplane and Tail Effects in Flapping Flight," in "42nd AIAA Fluid Dynamics Conference and Exhibit," New Orleans, 2012.

[21] Maybury, W., Rayner, J., and Couldrick, L., "Lift generation by the avian tail," *Philosophical Transactions of the Royal Society of London, Series B: Biological Sciences*, Vol. 268, 2001, pp. 1443–1448.

[22] Armanini, S., Caetano, J., de Visser, C., and de Croon, G., "Modelling wing wake and tail-wake interaction of a clap-and-peel flapping-wing MAV," in "AIAA Modeling and Simulation Technologies Conference," Grapevine, Texas, 2017.

[23] Caetano, J., de Visser, C., Remes, B., de Wagter, C., and Mulder, M., "Modeling a Flapping Wing MAV: Flight Path Reconstruction of the Delfly II," in "AIAA Modeling and Simulation Technologies (MST) Conference, Boston, MA.", , 2013.

[24] Caetano, J., de Visser, C., Remes, B., de Wagter, C., van Kampen, E.-J., and Mulder, M., "Controlled Flight Maneuvers of a Flapping Wing Micro Air Vehicle: a Step Towards the Delfly II Identification," in "2013 AIAA Atmospheric Flight Mechanics Conference," , 2013.

[25] Karásek, M., Koopmans, A., Armanini, S., Remes, B., and de Croon, G., "Free flight force estimation of a 23.5g flapping wing MAV using an on-board IMU," in "IEEE International Conference on Intelligent Robots and Systems (IROS)," Daejeon, Korea, 2016.

[26] Armanini, S., Karásek, M., de Croon, G., and de Visser, C., "Onboard/Offboard Sensor Fusion for High-Fidelity Flapping-Wing Robot Flight Data (in press)," *Journal of Guidance, Control, and Dynamics*.
[27] Armanini, S., de Visser, C., de Croon, G., and Mulder, M., "Time-Varying Model Identification of Flapping-Wing Vehicle Dynamics Using Flight Data," *Journal of Guidance, Control, and Dynamics*, Vol. 39, No. 3, 2016, pp. 526–541.
[28] Anderson, J. D., *Fundamentals of Aerodynamics*, McGraw Hill, 5th SI units ed., 2011.
[29] Percin, M., Eisma, H., van Oudheusden, B., Remes, B., Ruijsink, R., and de Wagter, C., "Flow visualization in the wake of flapping-wing MAV 'DelFly II' in forward flight," in "30th AIAA Applied Aerodynamics Conference," New Orleans, Louisiana, 2012.
[30] Caetano, J., Armanini, S., de Visser, C., de Croon, G., and Mulder, M., "Data-Informed Quasi-Steady Aerodynamic Model of a Clap-and-Fling Flapping Wing MAV," in "International Conference on Intelligent Unmanned Systems," Bali, Indonesia, 2015.
[31] Caetano, J., Percin, M., de Visser, C., van Oudheusden, B., de Croon, G., de Wagter, C., Remes, B., and Mulder, M., "Tethered vs. Free Flight Force Determination of the DelFly II Flapping Wing Micro Air Vehicle," in "2014 International Conference on Unmanned Aircraft Systems (ICUAS), Orlando, FL, USA," , 2014, pp. 942–948.
[32] Rose, C. and Fearing, R., "Comparison of Ornithopter Wind Tunnel Force Measurements with Free Flight," in "2014 IEEE International Conference on Robotics & Automation (ICRA)," Hong Kong, China, 2014.
[33] Armanini, S., de Visser, C., and de Croon, G., "Black-box LTI modeling of flapping-wing micro aerial vehicle dynamics," in "AIAA Atmospheric Flight Mechanics Conference," Kissimmee, Florida, 2015.
[34] Armanini, S., Caetano, J., de Visser, C., de Croon, G., and Mulder, M., "Aerodynamic Model Identification of a Clap-and-Fling Flapping-Wing MAV: a Comparison between Quasi-Steady and Black-Box Approaches," in "AIAA Atmospheric Flight Mechanics Conference," San Diego, California, USA, 2016.
[35] Ljung, L., *System Identification: Theory for the User*, Pearson Education (US), 2nd ed., 1998.
[36] Muijres, F., Spedding, G., Winter, Y., and Hedenström, A., "Actuator disk model and span efficiency of flapping flight in bats based on time-resolved PIV measurements," *Experiments in Fluids*, Vol. 51, 2011, pp. 511–525.